



24 **Abstract**

25 The precise contribution of the two major sinks for anthropogenic CO₂ emissions, terrestrial
26 vegetation and the ocean, and their location and year-to-year variability are not well understood.
27 Top-down estimates of the spatiotemporal variations in emissions and uptake of CO₂ are
28 expected to benefit from the increasing measurement density brought by recent in situ and
29 remote CO₂ observations. We uniquely apply a batch Bayesian synthesis inversion at relatively
30 high resolution to in situ surface observations and bias-corrected GOSAT satellite column CO₂
31 retrievals to deduce the global distributions of natural CO₂ fluxes during 2009-2010. Our
32 objectives include evaluating bottom-up prior flux estimates, assessing the value added by the
33 satellite data, and examining the impacts of inversion technique and assumptions on posterior
34 fluxes and uncertainties. The GOSAT inversion is generally better constrained than the in situ
35 inversion, with smaller posterior regional flux uncertainties and correlations, because of greater
36 spatial coverage, except over North America and high-latitude ocean. Complementarity of the in
37 situ and GOSAT data enhances uncertainty reductions in a joint inversion; however, spatial and
38 temporal gaps in sampling still limit the ability to accurately resolve fluxes down to the sub-
39 continental scale. The GOSAT inversion produces a shift in the global CO₂ sink from the tropics
40 to the north and south relative to the prior, and an increased source in the tropics of $\sim 2 \text{ Pg C y}^{-1}$
41 relative to the in situ inversion, similar to what is seen in studies using other inversion
42 approaches. This result may be driven by sampling and residual retrieval biases in the GOSAT
43 data, as suggested by significant discrepancies between posterior CO₂ distributions and surface
44 in situ and HIPPO mission aircraft data. While the shift in the global sink appears to be a robust
45 feature of the inversions, the partitioning of the sink between land and ocean in the inversions
46 using either in situ or GOSAT data is found to be sensitive to prior uncertainties because of



47 negative correlations in the flux errors. The GOSAT inversion indicates significantly less CO₂
48 uptake in summer of 2010 than in 2009 across northern regions, consistent with the impact of
49 observed severe heat waves and drought. However, observations from an in situ network in
50 Siberia imply that the GOSAT inversion exaggerates the 2010-2009 difference in uptake in that
51 region, while the prior CASA-GFED model of net ecosystem production and fire emissions
52 reasonably estimates that quantity. The prior, in situ posterior, and GOSAT posterior all indicate
53 greater uptake over North America in spring to early summer of 2010 than in 2009, consistent
54 with wetter conditions. The GOSAT inversion does not show the expected impact on fluxes of a
55 2010 drought in the Amazon; evaluation of posterior mole fractions against local aircraft profiles
56 suggests that time-varying GOSAT coverage can bias estimation of flux interannual variability in
57 this region.

58



59 1. Introduction

60 About one-half of the global CO₂ emissions from fossil fuel combustion and
61 deforestation accumulates in the atmosphere (Le Quéré et al., 2015), where it contributes to
62 global climate change. The rest is taken up by vegetation and the ocean. The precise
63 contribution of the two sinks, their location and year-to-year variability, and the environmental
64 controls on the variability are, however, not well understood. Top-down methods involving
65 atmospheric inverse modeling have been used extensively to quantify natural CO₂ fluxes (e.g.
66 Enting and Mansbridge, 1989; Ciais et al., 2010). An advantage of this approach over bottom-up
67 methods such as forest inventories (Pan et al., 2011; Hayes et al., 2012) or direct flux
68 measurements (Baldocchi et al., 2001; Chevallier et al., 2012) is that measurements of
69 atmospheric CO₂ mole fractions generally contain the influence of fluxes over a spatial scale
70 substantially larger than that of individual forest plots or flux measurements, so that errors from
71 extrapolating measurements to climatically relevant scales (e.g. ecosystem, sub-continental, or
72 global) are mitigated. However, the accuracy of top-down methods is limited by sparse data
73 coverage, uncertainties in atmospheric transport modeling, and mixing of signals from different
74 flux types such as anthropogenic and natural.

75 With the advent of retrievals of atmospheric CO₂ mole fraction from satellites, including
76 the Japanese Greenhouse gases Observing SATellite (GOSAT) (Yokota et al., 2009) and the
77 NASA Orbiting Carbon Observatory-2 (OCO-2) (Crisp, 2015), data coverage has improved
78 greatly. Making measurements since 2009, GOSAT is the first satellite in orbit designed
79 specifically to measure column mixing ratios of CO₂ (as well as methane) with substantial
80 sensitivity to the lower troposphere, close to surface fluxes. A number of modeling groups have
81 conducted CO₂ flux inversions using synthetic GOSAT data (Liu et al., 2014) and actual data



82 (Takagi et al., 2011; Maksyutov et al., 2013; Basu et al., 2013; Saeki et al., 2013a; Deng et al.,
83 2014; Chevallier et al., 2014; Takagi et al., 2014; Reuter et al., 2014; Houweling et al., 2015;
84 Deng et al., 2016). Unlike in situ measurements, which are calibrated directly for the gas of
85 interest, remote sensing involves challenges in precision and accuracy stemming from the
86 measuring of radiance. The retrievals rely on modeling of radiative transfer involving
87 complicated absorption and scattering by the atmosphere and reflection from the surface (e.g.
88 Connor et al., 2008; O'Dell et al., 2012). Passive measurements that rely on reflected sunlight
89 are more prone to errors than active measurements, as they are affected by not only errors related
90 to meteorological parameters and instrument noise but also systematic errors related to scattering
91 by clouds and aerosols, which can dominate the error budget (Kawa et al., 2010; O'Dell et al.,
92 2012). Furthermore, passive measurements have coverage gaps where there is insufficient
93 sunlight and where there is excessive scattering.

94 In addition to the model transport examined by a number of inversion intercomparison
95 studies (e.g. Gurney et al., 2002; Baker et al. 2006), the inversion technique and assumptions can
96 contribute to substantial differences in results. For example, Chevallier et al. (2014) found that
97 significant differences in hemispheric and regional flux estimates can stem from differences in
98 Bayesian inversion techniques, transport models, a priori flux estimates, and satellite CO₂
99 retrievals. Houweling et al. (2015) presented an intercomparison of 8 different inversions using
100 5 independent GOSAT retrievals, and also found substantial differences in optimized fluxes at
101 the regional level, with modeling differences (priors, transport, inversion technique) contributing
102 approximately as much to the spread in results on land as the different satellite retrievals used.

103 In this paper, we present inversions of GOSAT and in situ data using a distinct technique,
104 which are compared with results from other studies. All of the previous GOSAT satellite data



105 inversions have used computationally-efficient approaches, such as variational and ensemble
106 Kalman filter data assimilation, to handle the large amounts of data generated by satellites and
107 the relatively large number of flux regions whose estimation is enabled by such data. The
108 computational efficiency of these approaches results from numerical approximations. In this
109 study, we apply a traditional, batch, Bayesian synthesis inversion approach (e.g. Baker et al.,
110 2006) at relatively high spatiotemporal resolution to estimate global, interannually varying CO₂
111 fluxes from satellite and in situ data. Advantages of this technique include generation of an
112 exact solution along with a full-rank error covariance matrix (e.g. Chatterjee and Michalak,
113 2013), and an unlimited time window during which fluxes may influence observations, unlike
114 the limits typically imposed in Kalman filter techniques. The major disadvantages of the batch
115 technique are that computational requirements limit the spatiotemporal resolution at which the
116 inversion can be solved and the size of the data set that can be ingested, a large number of
117 transport model runs is required to pre-compute the basis functions (i.e. Jacobian matrix), and the
118 handling of the resulting volume of model output is very time-consuming at relatively high
119 resolution.

120 We estimate natural terrestrial and oceanic fluxes over the period May 2009 through
121 September 2010. The analysis spans two full boreal summers; longer periods were prohibited by
122 the computational effort. The objectives of this study are: 1) to understand recent variability of
123 the global carbon cycle, 2) to evaluate the bottom-up flux estimates used for the priors, 3) to
124 compare fluxes and uncertainties inferred using in situ observations, GOSAT observations, and
125 the two data sets combined and to assess the value added by the satellite data, and 4) to generate
126 inversion results using a unique Bayesian inversion technique for comparison with other
127 approaches.



128 Section 2 provides details on the inputs and inversion methods. Section 3 presents prior
129 and posterior model CO₂ mole fractions and their evaluation against independent data sets, fluxes
130 and uncertainties at various spatial and temporal scales, and comparisons with results from
131 inversions conducted by other groups. We discuss the robustness of results, and examine in
132 particular their sensitivity to assumed prior flux uncertainties. We then analyze the possible
133 impacts of several climatic events during the analysis period on CO₂ fluxes. Section 4 contains
134 concluding remarks.

135

136

137 2. Methods

138 Our method is based on that used in the TransCom 3 (TC3) CO₂ inversion
139 intercomparisons (Gurney et al., 2002; Baker et al. 2006) and that of Butler et al. (2010), the
140 latter representing an advance over the TC3 method in that they accounted for interannual
141 variations in transport and optimized fluxes at a higher spatial resolution. Our method involves
142 further advances over that of Butler et al. (2010), including higher spatial and temporal
143 resolution for the optimized fluxes, and the use of individual flask-air observations and daily
144 averages for continuous observations rather than monthly averages. Inversion theoretical studies
145 and intercomparisons have suggested that coarse resolution for flux optimization can produce
146 biased estimates, i.e. estimates that suffer from aggregation error (Kaminski et al., 2001; Engelen
147 et al., 2002; Gourdji et al., 2012). Although observation networks may not necessarily provide
148 sufficient constraints on fluxes at high resolutions, Gourdji et al. (2012) adopted the approach of
149 estimating fluxes first at fine scales and then aggregating to better-constrained resolutions to
150 minimize aggregation errors. The high spatiotemporal resolution of our inversion relative to



151 other Bayesian synthesis inversions would be expected to reduce aggregation errors. Similarly,
152 use of higher temporal resolution observations allows our inversion to more precisely capture
153 variability due to transport and thus more accurately estimate fluxes. Details on our inversion
154 methodology are provided in the sub-sections below.

155

156 2.1. A priori fluxes and uncertainties

157 Prior estimates for net ecosystem production (NEP = photosynthesis – respiration) and
158 fire emissions (wildfires, biomass burning, and biofuel burning) come from the Carnegie-Ames-
159 Stanford-Approach (CASA) biogeochemical model coupled to version 3 of the Global Fire
160 Emissions Database (GFED3) (Randerson et al., 1996; van der Werf et al., 2006; 2010). CASA-
161 GFED is driven with data on fraction of absorbed photosynthetically active radiation (FPAR)
162 derived from the AVHRR satellite series (Pinzon et al, 2014; Los et al., 2000), burned area from
163 MODIS (Giglio et al, 2010), and meteorology (precipitation, temperature, and solar radiation)
164 from the Modern-Era Retrospective Analysis for Research and Applications (MERRA)
165 (Rienecker et al., 2011). CASA-GFED fluxes are generated at $0.5^\circ \times 0.5^\circ$ resolution. For use in
166 the atmospheric transport model, monthly fluxes are downscaled to 3-hourly values using solar
167 radiation and temperature (Olsen and Randerson, 2004) along with MODIS 8-day satellite fire
168 detections (Giglio et al., 2006). In general, the biosphere is close to neutral in the CASA-GFED
169 simulation, i.e. there is no long-term net sink although there can be interannual variations in the
170 balance between uptake and release. In the version of CASA used here, a sink of $\sim 100 \text{ Tg C y}^{-1}$
171 is induced by crop harvest in the U.S. Midwest that is prescribed based on National Agriculture
172 Statistics Service data on crop area and harvest. Although respiration of the harvested products



173 is neglected, the underestimate of emissions that is implied is geographically dispersed and in
174 principle correctable by the inversion.

175 For air-sea CO₂ exchange, monthly, climatological, measurement-based fluxes are taken
176 from Takahashi et al. (2009) for the reference year 2000 on a 4° x 5° lat/lon grid. In contrast to
177 the CASA-GFED flux being close to neutral on a global basis, the prior ocean flux forms a net
178 sink of 1.4 Pg C y⁻¹. For fossil CO₂, 1° x 1°, monthly- and interannually-varying emissions are
179 taken from the Carbon Dioxide Information Analysis Center (CDIAC) inventory (Andres et al.,
180 2012). This includes CO₂ from cement production but not international shipping and aviation
181 emissions. Oxidation of reduced carbon-containing gases from fossil fuels in the atmosphere
182 (~5% of the emissions; Nassar et al., 2010) is neglected, and the entire amount of the emissions
183 is released as CO₂ at the surface. Similarly, CO₂ from oxidation of biogenic and biomass
184 burning gases is neglected. The total amount of CO₂ chemical production from fossil and
185 biospheric gases is estimated to be ~1 Pg C y⁻¹ (for year 2006; Nassar et al., 2010).

186 A priori flux uncertainties are derived from those assumed in the TC3 studies (Table 1),
187 rescaled to our smaller regions and shorter periods with the same approach as Feng et al. (2009).
188 A priori spatial and temporal error correlations are neglected in our standard inversions. The
189 neglect of a priori spatial error correlations is justified by the size of our flux optimization
190 regions, with dimensions on the order of one thousand to several thousand km, likely greater
191 than the error correlation lengths for our 2° x 2.5° grid-level fluxes. For example, Chevallier et
192 al. (2012) estimated a correlation e-folding length of ~500 km for a grid size close to ours of 300
193 km x 300 km based on comparison of a terrestrial ecosystem model with global flux tower data.

194

195 2.2. Observations and uncertainties



196 For constraining fluxes at relatively high temporal resolution, observations are chosen
197 that consist of discrete whole-air samples collected in glass flasks approximately weekly and
198 continuous in situ tall tower measurements of CO₂ mole fraction from the NOAA ESRL Carbon
199 Cycle Cooperative Global Air Sampling Network (Dlugokencky et al., 2013; Andrews et al.,
200 2009) supplemented with continuous ground-based measurements at 3 sites in East Asia from the
201 Japan Meteorological Agency (JMA) network ([http://ds.data.jma.go.jp/gmd/wdcgg/cgi-](http://ds.data.jma.go.jp/gmd/wdcgg/cgi-bin/wdcgg/catalogue.cgi)
202 [bin/wdcgg/catalogue.cgi](http://ds.data.jma.go.jp/gmd/wdcgg/catalogue.cgi), accessed 14 Mar 2013; Tsutsumi et al., 2006). Both data sets are
203 calibrated to the WMO-X2007 scale. In the present study, these data sets are referred to
204 collectively as “in situ” observations. The 87 sites (Fig. 1a) are chosen based on data availability
205 for the analysis period, Mar 2009-Sep 2010. Individual flask-air observations are used in the
206 inversions, and for the continuous measurements, afternoon averages are used (between 1200
207 and 1700 local standard time), avoiding the difficulty of simulating the effects of shallow
208 nighttime boundary layers. For the towers, data from the highest level only is used. We apply
209 minimal filtering of the data. For the NOAA data sets, we exclude only the data with “rejection”
210 flags, retaining data with “selection” flags (NOAA uses statistical filters and other information
211 such as wind direction to flag data that are likely valid but do not meet certain criteria such as
212 being representative of well-mixed, background conditions), since the relatively high-resolution
213 transport model used here (Sect. 2.3) captures much of the variability in the observations beyond
214 background levels. Furthermore, observations strongly influenced by local fluxes are typically
215 assigned larger uncertainties by our scheme (described below), and therefore have less weight in
216 the inversion. For the JMA data, we omit only the hourly data with flag = 0, meaning the
217 number of samples is below a certain level, the standard deviation is high, and there is a large
218 discrepancy with one or both adjacent hourly values. Although some of the observation sites



219 used in our inversion are located close to each other, there is never any exact overlap in grid box
220 (altitude and/or longitude-latitude) or in time. Thus, all of those sites are kept for the inversions,
221 with observations at each site and day treated as independent (i.e. neglecting error correlations).

222 We estimate the uncertainties for the flask-air observations as the root sum square (RSS)
223 of two uncertainty components: the standard deviation of the observations within a particular
224 hour (up to two pairs of duplicate samples) and a simple estimate of the model
225 transport/representation error. For the first uncertainty component, we assign a value of 0.3 ppm
226 if there is only one sample, and apply a minimum value of 0.01 ppm. The
227 transport/representation error estimation is similar to that of the NOAA CarbonTracker (CT) CO₂
228 data assimilation system (prior to the CT 2015 version) (Peters et al., 2007;
229 <http://carbontracker.noaa.gov>), whereby a fixed “model-data mismatch” is assigned based on the
230 type of site, e.g. marine, coastal, continental, or polluted, ranging from 0.4 ppm to 4 ppm. For
231 the continuous measurements, we take the RSS of two uncertainty components: the afternoon
232 root mean square (RMS) of the uncertainties of the 30-second or hourly average observations
233 reported by the data providers (divided by the square root of the number of observations, N), and
234 the standard error of all the 30-second/hourly mole fractions within an afternoon period. This
235 represents an attempt to account for instrument error as well as transport/representation error. In
236 addition, based on initial inversion results, we enlarged all in situ total observation uncertainties
237 by a factor of 2 to lower the normalized chi-squared (χ^2) value closer to 1 (the final value of
238 which is shown in Table 2).

239 GOSAT measures reflected sunlight in a sun-synchronous orbit with a 3-day repeat cycle
240 and a 10.5 km diameter footprint when in nadir mode (Yokota et al., 2009). The spacing
241 between soundings is ~250 km along-track and ~160 km or ~260 km cross-track (for 5-point/3-



242 point sampling before/after Aug 2010). We use the ACOS B3.4 retrieval of column-average
243 CO₂ dry air mole fraction (XCO₂), with data from June 2009 onward (O'Dell et al., 2012;
244 Osterman et al., 2013). Filtered and bias-corrected land nadir, including high (H) gain and
245 medium (M) gain, and ocean glint data are provided. Three truth metrics were used together to
246 correct biases (separately for H gain, M gain, and ocean glint) (Osterman et al., 2013; Lindqvist
247 et al., 2015; Kulawik et al., 2016): 1) an ensemble of transport model simulations optimized
248 against in situ observations, 2) coincident ground-based column observations from the Total
249 Carbon Column Observing Network (TCCON), which are calibrated to aircraft in situ profiles
250 linked to the WMO scale (Wunch et al., 2011), and 3) the assumption that CO₂ mole fraction
251 ought to exhibit little spatiotemporal variability in the Southern Hemisphere mid-latitudes other
252 than a seasonal cycle and long-term trend. For our inversions, we use the average of GOSAT
253 observations falling within a given 2° latitude × 2.5° longitude transport model column in a
254 given hour. Figure 1b shows the frequency of the ACOS GOSAT observations across the model
255 grid.

256 The values assumed for the GOSAT uncertainties are based in part on the retrieval
257 uncertainties provided with the ACOS data set. Following guidance from the data providers,
258 these are inflated by a factor of 2 over land and 1.25 over ocean for more realistic estimates of
259 the uncertainties (C. O'Dell, pers. comm., 2013); Kulawik et al. (2016) recommended an overall
260 scale factor of 1.9 for the similar ACOS B3.5 data set. In the case of multiple observations
261 within a model grid, we estimate the overall uncertainty as the RMS of the uncertainties of the
262 individual observations, divided by the square root of N. Error correlations between
263 observations in different model grids and at different hours are neglected.



264 Inversions are conducted using different combinations of data, including the in situ data
265 (“in situ-only”), the GOSAT data (“GOSAT-only”), and both (“in situ + GOSAT”).

266 We use several additional data sets for independent evaluation of the inversion results.
267 Aircraft measurements from the HIAPER Pole-to-Pole Observations (HIPPO) campaign consist
268 of vertical profiles of climate-relevant gases and aerosols from the surface to as high as the lower
269 stratosphere, spanning a wide range of latitudes mostly over the Pacific region (Wofsy et al.,
270 2011). Five missions were conducted during different seasons in 2009-2011, with two of the
271 missions overlapping with our analysis period. We use the “best available” CO₂ values derived
272 from multiple measurement systems from the merged 10-second data product (Wofsy et al.,
273 2012). Another data set, the ‘Amazonica’ aircraft measurements over the Amazon basin, is
274 useful for evaluating inversion performance over tropical land. These measurements consist of
275 profiles of several gases including CO₂ determined from flask samples from just above the forest
276 canopy to 4.4 km altitude over 4 sites across the Brazilian Amazon starting in 2010, taken
277 approximately biweekly (Gatti et al., 2014, 2016). Finally, the Japan-Russia Siberian Tall Tower
278 Inland Observation Network (JR-STATION) of towers provides continuous in situ
279 measurements of CO₂ and CH₄ over different ecosystem types across Siberia beginning in 2002
280 (Sasakawa et al., 2010; Sasakawa et al., 2013). The JR-STATION data have been used in
281 combination with other in situ observations in CO₂ flux inversions (Saeki et al., 2013b; Kim et
282 al., 2017).

283

284 2.3. Atmospheric transport model and model sampling

285 We use the Parameterized Chemistry and Transport Model (PCTM) (Kawa et al., 2004),
286 with meteorology from the NASA Global Modeling and Assimilation Office (GMAO) MERRA



287 reanalysis (Rienecker et al., 2011). For this analysis, PCTM was run at a resolution of 2° latitude
288 × 2.5° longitude and 56 hybrid terrain-following levels up to 0.4 hPa. A “pressure fixer” scheme
289 has been implemented to ensure tracer mass conservation, the lack of which can be a significant
290 problem with assimilated winds (Kawa et al., 2004). This version of PCTM was among the
291 transport models that participated in TransCom intercomparisons (Gurney et al., 2005; Law et
292 al., 2008).

293 Offshore prior terrestrial biospheric and fossil fluxes are redistributed to the nearest
294 onshore grid cells in the model grid to counteract diffusion caused by our regridding the original
295 fluxes to the coarser 2° × 2.5° resolution, as recommended in the TC3 protocol (Gurney et al.,
296 2000).

297 The model is initialized with a concentration field appropriate for March 22, 2009 from a
298 multi-year PCTM run with prior fluxes. The initial conditions are optimized in the inversions, as
299 described in Sect. 2.4.

300 PCTM is sampled at grid cells containing in situ observation sites or GOSAT soundings,
301 at the hours corresponding to the observations. To mimic the sampling protocol for coastal flask
302 sites, which favors clean, onshore wind conditions, the model is sampled at the neighboring
303 offshore grid cell if the cell containing the site is considered land according to a land/ocean
304 mask. For in situ sites in general, the appropriate vertical level as well as horizontal location is
305 selected. Specifically, the model CO₂ profile is interpolated to the level corresponding on
306 average to the altitude above sea level of the observation site. This procedure is relevant
307 primarily for mountain sites and tall towers as well as aircraft samples; the lowest model level
308 was used for most other sites.



309 Model columns are weighted using ACOS column averaging kernels applied to
310 deviations of model CO₂ profiles from ACOS a priori profiles (Connor et al., 2008).

311 Time series of model and observed mole fractions at selected flask and continuous sites
312 spanning a range of latitudes, longitudes, elevations, and proximity to major fluxes are shown for
313 the prior and for the in situ-only inversion in Fig. 2. The prior model as well as the in situ
314 inversion captures much of the observed synoptic-scale variability. This suggests that the PCTM
315 transport is reasonably accurate, consistent with the findings of Parazoo et al. (2008) and Law et
316 al. (2008).

317

318 2.4. Inversion approach

319 The batch, Bayesian synthesis inversion approach optimizes in a single step the
320 agreement between model and observed CO₂ mole fractions and between a priori and a posteriori
321 flux estimates in a least-squares manner (e.g. Enting et al., 1995). As in the paper by Baker et al.
322 (2006), the cost function minimized in this approach can be expressed as

323

$$324 J = (\mathbf{c}_{\text{obs}} - \mathbf{c}_{\text{fwd}} - \mathbf{H}\mathbf{x})^T \mathbf{R}^{-1} (\mathbf{c}_{\text{obs}} - \mathbf{c}_{\text{fwd}} - \mathbf{H}\mathbf{x}) + (\mathbf{x}_0 - \mathbf{x})^T \mathbf{P}_0^{-1} (\mathbf{x}_0 - \mathbf{x}), \quad (1)$$

325

326 where $\mathbf{c}_{\text{obs}} - \mathbf{c}_{\text{fwd}}$ are mismatches between the observations and the mole fractions produced by
327 the prior fluxes, \mathbf{H} is the Jacobian matrix relating model mole fractions at the observation
328 locations to regional flux adjustments \mathbf{x} , \mathbf{R} is the covariance matrix for the errors in $\mathbf{c}_{\text{obs}} - \mathbf{c}_{\text{fwd}}$,
329 \mathbf{x}_0 is an a priori estimate of the flux adjustments, and \mathbf{P}_0 is the covariance matrix for the errors in
330 \mathbf{x}_0 . The solution for the a posteriori flux adjustments, $\hat{\mathbf{x}}$, is

331



332 $\hat{\mathbf{x}} = (\mathbf{H}^T \mathbf{R}^{-1} \mathbf{H} + \mathbf{P}_0^{-1})^{-1} (\mathbf{H}^T \mathbf{R}^{-1} (\mathbf{c}_{\text{obs}} - \mathbf{c}_{\text{fwd}}) + \mathbf{P}_0^{-1} \mathbf{x}_0),$ (2)

333

334 and the a posteriori error covariance matrix is given by

335

336 $\mathbf{P} = (\mathbf{H}^T \mathbf{R}^{-1} \mathbf{H} + \mathbf{P}_0^{-1})^{-1}.$ (3)

337

338 This study focuses on the variability of natural fluxes (terrestrial NEP and ocean), and
339 thus considers adjustments to those fluxes only, assuming the prior estimates for the fossil and
340 fire fluxes are correct. This is commonly done in CO₂ inversion studies (e.g. Gurney et al., 2002;
341 Peters et al., 2007; Basu et al., 2013), with the rationale that the anthropogenic emissions are
342 relatively well known, at least at the coarse spatial scales of most global inversions. In our
343 inversion, flux adjustments are solved for at a resolution of 8 days and for each of 108 regions
344 that are modified from the 144 regions of Feng et al. (2009) (Fig. 1a), which are in turn
345 subdivided from the TC3 regions. (The choice of an 8-day flux interval is based on data
346 considerations, e.g. the quasi-weekly frequency of the flask measurements and reasonable
347 sampling by GOSAT.) This is a significantly higher resolution than the monthly intervals and
348 22/47 regions in the previous batch inversions of TC3/Butler et al. (2010). One of our regions
349 consists of low-flux land areas (e.g. Greenland, Antarctica) as well as small offshore areas that
350 contain non-zero terrestrial biospheric fluxes but do not fit into any of the TC3-based land
351 regions, similar to what was done by Feng et al. (2009). We also created a region that includes
352 areas with non-zero oceanic fluxes that do not fit into any of the TC3-based ocean regions
353 according to our gridding scheme.



354 Grid-scale spatial patterns are imposed in our flux adjustments based on the natural
355 fluxes, similar to TC3 and Butler et al. (2010), except that we use patterns specific to our prior
356 NEP or air-sea flux averaged over each particular 8-day period, rather than annual mean net
357 primary productivity (NPP) patterns over land and spatially constant patterns over the ocean. To
358 ensure net changes in flux are possible across each region, absolute values are used for the flux
359 patterns. Prior values of 0 are specified for all flux adjustments.

360 The initial conditions (i.c.) are also optimized at the same time as the fluxes via two
361 parameters: a scale factor to the i.c. tracer (described below) that allows for overall adjustment
362 of spatial gradients, and a globally uniform offset. A priori uncertainties of 0.01 for the scale
363 factor and 30 ppm for the offset are prescribed. Inversion results from March 22 through April
364 30, 2009 are discarded to avoid the influence of any inaccuracies in the initial conditions. (Our
365 tests showed that inferred fluxes after the first two months are insensitive to the treatment of i.c.)
366 Although the GOSAT data set begins in June 2009, the observations can provide some constraint
367 on earlier fluxes.

368 For generating the prior mole fractions, \mathbf{c}_{fwd} , and constructing the Jacobian matrix, \mathbf{H} ,
369 transport model runs were performed for each of the prior flux types and an i.c. tracer, as well as
370 a run with a flux pulse (normalized to 1 Pg C y^{-1}) for each of the 108 regions and 71 8-day
371 periods. (The last period in 2009 is shortened to 5 days to fit cleanly within the year.) The i.c.
372 tracer is initialized as described in Sect. 2.3 and transported without emissions or removals for
373 the duration of the analysis period. Each flux pulse is transported for up to 13 months, after
374 which the atmosphere is well mixed (within a range of 0.01 ppm). This procedure generated a
375 massive amount of 3-D model output, ~30 terabytes (compressed). All of the model output was
376 then sampled at the observation locations and times.



377 A singular value decomposition (SVD) approach is used to obtain a stable inversion
378 solution (Rayner et al., 1999). Use of the SVD technique is especially helpful in the case of the
379 inversions using GOSAT data, since the Jacobian matrix is too large to be successfully inverted
380 on our system (with a single CPU).

381

382

383 **3. Results**

384 3.1. General evaluation of inversions, including short-term flux variability

385 Posterior model mole fractions are closer to the assimilated observations than are the
386 prior mole fractions for the in situ-only, GOSAT-only, and in situ + GOSAT inversions, as
387 desired, as suggested by Fig. 2 and indicated by the means and standard deviations of the model-
388 observation differences over all observations shown in Fig. 3 (a, d, e, and f). Comparison of
389 posterior mole fractions with the data set not used (Fig. 3b, c), on the other hand, gives mean
390 differences not as close to 0 as in the comparison with the assimilated data, and standard
391 deviations that are larger than for the prior; this reflects the fact that the in situ and GOSAT data
392 sets are not necessarily consistent with each other and have independent random errors. The
393 improved agreement between model and assimilated observations is reflected also in the chi-
394 squared (cost function) values before and after the inversions shown in Table 2. The expected
395 value of chi-squared (normalized) for a satisfactory inversion is 1, which signifies that the
396 tightness of the fit of the results to the observations and to the a priori parameter estimates is
397 comparable to the level of uncertainty assumed for the observations and the a priori estimates.
398 The posterior chi-squared values for all of the inversions are closer to 1 than the prior values.



399 In addition to cross-evaluating the in situ-only and GOSAT-only inversions, we evaluate
400 both inversions against the independent, well-calibrated Amazon aircraft data set, which samples
401 an under-observed region with large, variable fluxes. Vertical profiles of the model and the
402 aircraft data (Fig. S1 in the supplementary material) show that the prior mole fractions often
403 exhibit a bias relative to the aircraft observations, especially in a boundary layer-like structure
404 below ~2 km altitude, with the sign of the average bias varying from season to season. The in
405 situ inversion often exhibits worse agreement with the observations than the prior does (with a
406 root mean square error (RMSE) that is more than 1 ppm larger in 27 of 60 cases above 2 km, and
407 in 27 cases below 2 km). The GOSAT inversion not only exhibits smaller discrepancies with the
408 observations than the in situ inversion does in general (29 of 60 cases above 2 km and 28 cases
409 below 2 km, while the reverse is true in only 11 cases above 2 km and 25 cases below 2 km), but
410 it also is more often better than the prior than worse above 2 km (16 vs. 13 cases). In contrast,
411 the in situ inversion is more often worse than the prior than better (e.g. 27 vs. 12 cases above 2
412 km). Overall statistics, computed separately for lower and higher altitudes, are shown in Fig. 4.
413 The model-observation histograms indicate that agreement with the aircraft observations is again
414 better for the GOSAT inversion than the in situ inversion, with smaller or comparable mean
415 differences and standard deviations. There is a near complete lack of in situ sites in the inversion
416 that are sensitive to Amazon fluxes (as suggested by Fig. 1a), contrasting with the availability of
417 some GOSAT data over the region (Fig. 1b), meaning that regional flux adjustments in the in situ
418 inversion are driven, often erroneously, by correlations with fluxes outside of the region (as will
419 be discussed in depth below in Sect. 3.3). The GOSAT inversion agrees with the aircraft
420 observations better than the prior does above 2 km, implying that incorporating GOSAT data in
421 the inversion results in better performance than no data. However, the posterior model-



422 observation differences have greater variance than the prior below 2 km. A possible explanation
423 for this is that the use of GOSAT observations in an inversion introduces more random error in
424 the model mole fractions, which would not be expected to be correlated with the aircraft
425 measurement error. GOSAT errors presumably affect higher altitudes in the model less, since
426 the mole fractions there are influenced by fluxes across a broader area than at lower altitudes and
427 thus errors are averaged out to a greater extent.

428 Example time series of 8-day mean prior and posterior NEP and ocean fluxes for the in
429 situ-only and GOSAT-only inversions are shown in Fig. 5. Since the posterior fluxes in our
430 inversion regions tend to have large fractional uncertainties, especially for the in situ-only
431 inversion, we focus in this paper on results aggregated to larger regions. To facilitate
432 comparison with other studies, results are aggregated to TC3 land and ocean regions, accounting
433 for error correlations. The posterior time series exhibit larger fluctuations than the prior time
434 series, especially for the in situ inversion over land. The fluctuations would presumably be
435 smaller if we excluded flagged, outlier in situ observations or used a smoothed data product such
436 as GLOBALVIEW-CO₂ (2009), which has been used in many inversions including those of TC3
437 and some of those in the Houweling et al. (2015) intercomparison. In addition, some of the
438 fluctuations likely represent actual variability in the fluxes, while other fluctuations are probably
439 noise. In fact, the calculated numbers of degrees of freedom for signal and noise (as defined by
440 Rodgers, 2000) are 3525 and 4186 for the in situ inversion (summing up approximately to the
441 number of inversion parameters, 7674) and 4925 and 2947 for the GOSAT inversion. This
442 indicates that ~45% of the in situ inversion solution is based on actual information from the
443 measurements, given the assumed prior and observation uncertainties, while ~65% of the
444 GOSAT inversion solution is constrained by the measurements. The in situ data set is sparser



445 than GOSAT, especially over land, and thus contains greater spatial sampling bias, so that many
446 of the flux regions are under-determined and may exhibit so-called dipole behavior associated
447 with negative error correlations (discussed further below).

448 Results for the in situ + GOSAT inversion (not shown in Fig. 5) lie mostly in between the
449 in situ-only and GOSAT-only results. The fluxes generally lie closer to those of the GOSAT-
450 only inversion for regions with a relatively low density of in situ measurements, including
451 tropical and southern land regions, while they lie closer to those of the in situ-only inversion for
452 regions with a relatively high density of in situ measurements, including northern land and many
453 ocean regions.

454 To average out noise in the posterior fluxes and to better observe the major features in the
455 results, we show monthly average fluxes in Fig. 6. There is a similar onset of seasonal CO₂
456 drawdown in the GOSAT-only inversion and the CASA-GFED prior in Boreal North America,
457 Temperate North America, and Boreal Asia, whereas the in situ-only inversion is noisier, similar
458 to what was noted above. The GOSAT inversion suggests an overall shift in the global CO₂ sink
459 from tropical and southern land to northern land regions relative to the prior and the in situ
460 inversion, similar to what has been found in previous GOSAT inversions (e.g. Houweling et al.,
461 2015; discussed further below). There are some unusual features in the GOSAT inversion. For
462 example, there is a negative flux in January in some northern regions, with the 1 σ range lying
463 entirely below zero for Boreal Asia and Europe; this CO₂ uptake does not seem plausible in the
464 middle of winter for these regions. Also, there are large positive fluxes during winter through
465 spring in Northern Africa, which deviate from the prior beyond any overlap in the 1 σ ranges for
466 two months and whose 1 σ ranges stay above zero for six months, summing up to a source of 1.9
467 Pg C over the period December through May, not including fires. The fluxes are larger than



468 those of any sustained period of positive fluxes in any region in either the prior or the in situ
469 inversion. The anomalous features suggest that the GOSAT inversion is affected by uncorrected
470 retrieval biases that vary by season and region (as has been shown by Lindqvist et al. (2015) and
471 Kulawik et al. (2016)) and/or sampling biases, including a lack of observations at high latitudes
472 during winter, which limit the ability to accurately resolve inferred fluxes down to the scale of
473 TransCom regions.

474 A comparison of the monthly mean fluxes with those from another inversion system,
475 NOAA's CarbonTracker version 2013B (CT2013B), is displayed in Fig. 7. CT2013B is an
476 ensemble Kalman smoother data assimilation system with a window length of five weeks that
477 uses multiple in situ observation networks and prior models to optimize weekly fluxes (Peters et
478 al., 2007; https://www.esrl.noaa.gov/gmd/ccgg/carbontracker/CT2013B/CT2013B_doc.php,
479 accessed 4 October 2016). Similar to the present study, CT2013B uses CASA-GFED3 fluxes
480 from van der Werf et al. (2010) as one of the land NEP priors, though with different FPAR and
481 meteorological driver data. (CASA-GFED2 is the other land prior in its ensemble of priors.) In
482 addition, CT2013B uses the seawater $p\text{CO}_2$ distribution from the Takahashi et al. (2009)
483 climatology to compute fluxes for one of its ocean priors; the other ocean prior is based on
484 results from an atmosphere-ocean inversion. CT2013B uses 93 observation time series while 87
485 are used here, although the former include measurements by multiple labs at the same site and
486 flask and continuous measurements at the same site (where duplicate observations are de-
487 weighted by inflating the model-data mismatch error by the square root of N). A notable
488 difference is that CT2013B solves for uniform flux scale factors over entire ecosystem types
489 within each TC3 region, with the ecosystem types not necessarily being contiguous. Results
490 from our in situ-only inversion are shown alongside those of CT2013B in Fig. 7 aggregated over



491 large regions. The two sets of posterior flux time series are similar overall, with overlapping 2σ
492 ranges at all times except in the Northern Oceans region. One distinctive feature is that the
493 posterior fluxes stay closer to the priors for CT2013B. A likely explanation is the tighter prior
494 uncertainties in CT2013B, the magnitudes of which are on average 40% of ours for land regions
495 and 30% of ours for ocean regions. For its ocean prior based on an atmosphere-ocean inversion,
496 CT2013B assumes uncertainties consistent with the formal *posterior* uncertainties from the
497 inversion, which are relatively small because of the large number of ocean observations used in
498 the inversion; uniform fractional uncertainties are assumed for the other ocean prior and the land
499 priors. Another feature is the larger month-to-month fluctuations in our results. A number of
500 factors could contribute to smaller fluctuations in the CT2013B results. One of them is the
501 tighter prior uncertainties used. Another factor is the use of prior estimates that represent a
502 smoothing over three assimilation time steps, which attenuates variations in the forecast of the
503 flux parameters in time. And another is that to dampen spurious noise due to the approximation
504 of the covariance matrix by a limited ensemble, CT2013B applies localization for observation
505 sites outside of the marine boundary layer, in which flux parameters that have a non-significant
506 relationship with a particular observation are excluded. We further evaluate our inversions in the
507 following sections.

508

509 3.2. Longer-term budgets and observation biases

510 Longer-timescale budgets can be assessed in Fig. 8, which displays 12-month mean
511 fluxes (Jun 2009-May 2010) over large, aggregated regions, with fires now included, for our
512 inversions and the CT2013B inversion. Results for individual TC3 regions are shown in Table 1.
513 The global total flux (including fossil emissions) is substantially more positive for the GOSAT-



514 only inversion relative to the in situ-only inversion, $6.5 \pm 0.2 \text{ Pg C y}^{-1}$ vs. $4.1 \pm 0.5 \text{ Pg C y}^{-1}$,
515 while that for the in situ + GOSAT inversion lies in between at $5.7 \pm 0.2 \text{ Pg C y}^{-1}$. Such a large
516 difference in the atmospheric CO_2 growth rate implied by the two distinct data sets is plausible
517 even if there are no trends in uncorrected biases between the data sets, given their sampling of
518 different regions of the atmosphere and the relatively short 12-month time frame over which the
519 growth occurs. In fact, for a different 12-month period within our analysis, Sep 2009-Aug 2010,
520 the total fluxes for the GOSAT-only and in situ-only inversions are much closer to each other—
521 5.53 Pg C y^{-1} and 5.47 Pg C y^{-1} . Houweling et al. (2015) also found a larger total flux in the
522 GOSAT-only inversions relative to the in situ during Jun 2009-May 2010 averaged across 8
523 models, $\sim 4.8 \text{ Pg C y}^{-1}$ vs. $\sim 4.6 \text{ Pg C y}^{-1}$, though the difference may not be statistically
524 significant.

525 As was noted earlier in this section, the GOSAT-only inversion exhibits a shift in the
526 global CO_2 sink from tropical and southern land to northern land relative to the prior and the in
527 situ-only inversion (Fig. 8). The differences are within the 1σ uncertainty ranges. The shift
528 includes an increase in the source in N. Africa ($0.2/1.5/2.0 \text{ Pg C y}^{-1}$ for prior/in situ-
529 only/GOSAT-only), Temperate S. America ($0.4/0.4/1.1 \text{ Pg C y}^{-1}$), and Australia ($0.0/-0.2/0.6 \text{ Pg}$
530 C y^{-1}), and an increase in the sink in Europe ($-0.1/0.6/-1.5 \text{ Pg C y}^{-1}$) and Temperate N. America
531 ($-0.3/-0.6/-1.5 \text{ Pg C y}^{-1}$) (Table 1). As for the ocean, the GOSAT inversion also exhibits a larger
532 source in the tropics relative to the prior and the in situ inversion (outside of the 1σ ranges; Fig.
533 8). However, the GOSAT inversion now exhibits a smaller sink over northern ocean relative to
534 the in situ inversion, and a larger sink over southern ocean relative to both the prior and the in
535 situ inversion (at or outside of the 1σ ranges). The TC3 regions contributing the most to these
536 differences include Tropical Indian ($0.1/0.0/0.7 \text{ Pg C y}^{-1}$ for prior/in situ-only/GOSAT-only), N.



537 Pacific ($-0.9/-0.5$ Pg C y^{-1} for in situ-only/GOSAT-only), N. Atlantic ($-0.8/-0.5$ Pg C y^{-1} for in
538 situ-only/GOSAT-only), and Southern Ocean ($-0.2/-0.4/-0.9$ Pg C y^{-1} for prior/in situ-
539 only/GOSAT-only) (Table 1).

540 The GOSAT results appear to contradict global carbon cycle studies that favor a weaker
541 terrestrial net source in the tropics compensated by a weaker northern extratropical sink (e.g.
542 Stephens et al., 2007; Schimel et al., 2015). However, the shift may be due at least in part to
543 GOSAT retrieval and sampling biases. An evaluation of posterior mole fractions in the GOSAT-
544 only inversion against surface in situ observations indicates that the GOSAT inversion may be
545 biased low during much of the analysis period over Europe and Temperate N. America,
546 especially in winter (when there is little direct constraint at high latitudes by GOSAT
547 observations), and biased somewhat high over N. Africa, especially in spring. However, the
548 dearth of in situ sites over N. Africa, with only one in the middle of the region (Assekrem,
549 Algeria) and a few around the edges (e.g. Izaña, Canary Islands and Mt. Kenya, Kenya),
550 precludes a definitive evaluation over that region. Globally, the GOSAT inversion tends to
551 underestimate mole fractions at high latitudes of the Northern Hemisphere, often by more than
552 1σ , as shown by latitudinal profiles averaged over all surface sites by season (Fig. 9), suggesting
553 an overestimated northern sink. The same is true of the high latitudes of the Southern
554 Hemisphere. The GOSAT inversion overestimates mole fractions in parts of the tropics,
555 sometimes by more than 1σ (Fig. 9), suggesting an overestimated tropical source. Uncorrected
556 retrieval biases may be especially prevalent in the tropics, where there are very few TCCON
557 stations available as input to the GOSAT bias correction formulas; only 1 TCCON station,
558 Darwin, Australia, was operating in the tropics during 2009-2010, and only 2 more stations,
559 Reunion Island and Ascension Island, became operational during the rest of the ACOS B3.4



560 retrieval period. In contrast, the posterior mole fractions for the in situ-only inversion generally
561 agree well with the surface observations (Fig. 9; also seen in the individual site time series in
562 Fig. 2), which is expected given that these are the observations that are used in the optimization.
563 The prior mole fractions are generally too high, which is consistent with the fact that the CASA-
564 GFED biosphere is near neutral while the actual terrestrial biosphere is thought to generally be a
565 net CO₂ sink.

566 Evaluation of the inversions against latitudinal profiles constructed from HIPPO aircraft
567 measurements, which provide additional sampling over the Pacific, indicates an overestimate by
568 the GOSAT inversion relative to HIPPO in parts of the tropics at lower altitudes (Fig. 10a, d),
569 similar to what was seen in the comparison with surface observations. And the GOSAT
570 inversion exhibits an underestimate relative to HIPPO in the southern extratropics in the lower to
571 middle levels of the troposphere (Fig. 10a, b, d, e), especially for Mission 2 (Oct-Nov 2009).
572 Again, the lack of GOSAT ocean observations at southern high latitudes points to sampling bias
573 as the cause of the underestimate. In the northern extratropics, the comparison of the inversions
574 with HIPPO has different features from the comparison with surface data: the GOSAT inversion
575 generally exhibits higher mean mixing ratios than HIPPO in the lower troposphere, especially for
576 Mission 2, and the in situ inversion gives higher mixing ratios at some latitudes in the northern
577 extratropics and lower mixing ratios at others for Mission 2. In one particular latitude range, 55-
578 67°N, both inversions give much higher mixing ratios than HIPPO, by up to 67 ppm in the case
579 of the in situ inversion and 30 ppm for the GOSAT inversion. This could reflect inaccuracy in
580 posterior fluxes due to the inversions' being under-constrained over the high-latitude North
581 Pacific and Alaska, with few observations during this season in the case of GOSAT and a
582 tendency for the sparse in situ network to produce noisy inversion results, as was discussed



583 above. However, given that the prior model also gives substantially higher mixing ratios than
584 HIPPO at these latitudes (by up to 11 ppm), the discrepancy could be due in part to transport
585 error.

586 In the upper troposphere to lower stratosphere, the GOSAT inversion more often than not
587 exhibits better agreement with the HIPPO observations than the in situ inversion does for both
588 Mission 2 and 3 (Fig. 10c, f). A likely explanation is that the GOSAT data provide constraints
589 throughout the atmospheric column, whereas the in situ measurements constrain only surface
590 CO₂. Figure 10 shows that the high-altitude mole fractions from the in situ inversion are
591 consistently close to those of the prior, suggesting that the lack of high-altitude constraints
592 prevents major adjustments in mole fractions at these levels, unlike in the GOSAT inversion.
593 Although GOSAT biases may affect these altitudes as well, it appears to be the case that the data
594 still provide better constraints than no observations above the surface at all. Furthermore, an air
595 parcel at higher altitudes, especially in the upper troposphere or above, generally consists of a
596 mixture of air originating from a broad area near the surface (e.g. Orbe et al., 2013), and thus the
597 effects of different regional biases in posterior fluxes may cancel out at those altitudes.

598 The conclusion that GOSAT biases may contribute to the shift in the land sink is also
599 supported by Houweling et al. (2015). That study reported a shift in the GOSAT-only inversions
600 relative to the in situ inversions consisting of an increase in the sink in northern extratropical
601 land of 1.0 Pg C y⁻¹ averaged across models and an increase in the source in tropical land of 1.2
602 Pg C y⁻¹ during June 2009-May 2010; in comparison, our inversions produce an increase in the
603 northern land sink of 0.4 Pg C y⁻¹ and an increase in the tropical land source of 1.2 Pg C y⁻¹ (Fig.
604 8). Houweling et al. (2015) found an especially large and systematic shift in flux of ~0.8 Pg C y⁻¹
605 between N. Africa and Europe, but then provided evidence that the associated latitudinal



606 gradient in CO₂ mole fractions may be inconsistent with that based on surface and HIPPO
607 aircraft in situ observations. They also suggested that the shift in annual flux between the two
608 regions may be a consequence of sampling bias, with a lack of GOSAT observations at high
609 latitudes during winter. Chevallier et al. (2014) also found a large source in N. Africa of ~1 Pg C
610 y⁻¹ in their ensemble of GOSAT inversions and considered the magnitude of that unrealistic,
611 given that emissions from fires in that region likely amount to < 0.7 Pg C y⁻¹. (Note that our N.
612 Africa source is even larger than that of Chevallier et al. (2014).) An observing system
613 simulation experiment by Liu et al. (2014) found that GOSAT seasonal and diurnal sampling
614 biases alone could result in an overestimated annual sink in northern high-latitude land regions.
615 Again, the results for the in situ + GOSAT inversion lie mostly in between those for the
616 in situ-only and GOSAT-only inversions, with the in situ + GOSAT fluxes lying closer to the
617 GOSAT-only ones for the tropical/southern land regions and land as a whole (Table 1 and Fig.
618 8), suggesting the dominance of the GOSAT constraint in these regions. The posterior
619 uncertainties for the GOSAT inversion (Table 1) are as small as or smaller than those for the in
620 situ inversion, except in Boreal and Temperate N. America, N. Pacific, Northern Ocean, and
621 Southern Ocean. This reflects the fact that GOSAT generally provides better spatial coverage,
622 except over N. America, where the in situ network provides good coverage, and over and near
623 high-latitude ocean areas, where there is decent in situ coverage and poor GOSAT coverage.
624 Uncertainty reductions in the in situ inversion range from 15% to 93% for land regions and 15%
625 to 56% for ocean regions (Table 1). In the GOSAT inversion, the uncertainty reductions range
626 from 43% to 89% for land and 19% to 56% for ocean. And in the inversion with combined in
627 situ and GOSAT data, the uncertainty reductions are larger than or equal to those in either the in



628 situ-only or the GOSAT-only inversion, ranging from 61% to 96% for land and 40% to 67% for
629 ocean.

630

631 3.3. Flux error correlations and land-ocean partitioning

632 Here we elaborate on the subject of posterior error correlations, which indicate the degree
633 to which fluxes are estimated independently of one another. Negative correlations can be
634 manifested in dipole behavior, in which unusually large flux adjustments of opposite signs occur
635 in neighboring regions/time intervals. These are shown in Fig. 11 aggregated to TC3 regions and
636 the 12-month period from June 2009 to May 2010. The full-rank error covariance matrix
637 generated by the exact Bayesian inversion method (from which the correlation coefficients are
638 derived) is a unique product of this study, particularly as applied to satellite data. There are a
639 larger number of sizable correlations between land regions in the in situ inversion than in the
640 GOSAT inversion (in the top left quadrants of the plots). One specific feature is negative
641 correlations among the four TC3 regions in South America and Africa in the in situ inversion,
642 whereas in the GOSAT inversion there are negative correlations within South America and
643 within Africa but not between the two continents. In contrast, the GOSAT inversion exhibits
644 larger anti-correlations over the ocean regions. For example, there are substantial negative
645 correlations between Southern Ocean and each of the other southern regions—S. Pacific, S.
646 Atlantic, and S. Indian. This is consistent with the almost complete lack of GOSAT observations
647 at the latitudes of the Southern Ocean region and the southern edges of the neighboring ocean
648 regions (Fig. 1b). Interestingly, there is not a sizable correlation between N. Africa and Europe
649 in the GOSAT inversion (in either seasonal or 12-month means), which runs counter to what
650 might be expected from the shift in flux discussed above; rather, each of these regions is



651 correlated with a number of other regions. We do find a fairly large correlation of -0.62 between
652 the northern extratropics in aggregate (land + ocean) and the tropics for the 12-month period
653 though. Correlations for the in situ + GOSAT inversion (not shown) generally lie in between
654 those of the in situ-only and GOSAT-only inversions. Even with the incorporation of both sets
655 of observations, there are substantial correlations of as much as -0.6 between regions within a
656 continent, reinforcing our earlier conclusion that sampling gaps limit the ability of the
657 observations to constrain fluxes down to the scale of most TC3 regions.

658 The in situ-only and CT2013B posterior global totals are nearly the same, but the land-
659 ocean split is different, with our inversion exhibiting a larger sink over ocean than over land
660 (with non-overlapping 2σ ranges) while in CT2013B the land and ocean fluxes are similar, with
661 the ocean flux changing little from the prior (Fig. 8). A likely explanation for the difference is
662 the very tight prior constraints on ocean fluxes of CT2013B that were discussed above, which
663 force the flux adjustments to take place mostly on land. The GOSAT inversion also exhibits a
664 relatively large ocean sink of $-3.1 \pm 0.5 \text{ Pg C y}^{-1}$; for comparison, the CT2013B estimate is $-2.4 \pm$
665 0.4 Pg C y^{-1} , our in situ-only estimate is $-4.0 \pm 0.8 \text{ Pg C y}^{-1}$, and the estimate of the Global
666 Carbon Project (GCP) is $-2.5 \pm 0.5 \text{ Pg C y}^{-1}$ for 2009-2010 (Le Quéré et al., 2013; Le Quéré et
667 al., 2015). The GCP estimate is a synthesis that combines indirect observation-based estimates
668 for the mean over the 1990s with interannual variability from a set of ocean models and accounts
669 for additional observation-based estimates in the uncertainty. The difference between our
670 inversion estimates and the GCP estimate is actually even larger than suggested by those
671 numbers, given that a background river to ocean flux of $\sim 0.5 \text{ Pg C y}^{-1}$ should be subtracted from
672 our ocean flux to make it comparable to the GCP ocean sink, which refers to net uptake of
673 *anthropogenic* CO_2 (Le Quéré et al., 2015). Similarly, in comparing our results with those of



674 Houweling et al. (2015), we find that the global budgets are comparable for all three
675 inversions—in situ-only, GOSAT-only, and in situ + GOSAT—as was mentioned above, but the
676 land-ocean split is different. Our posterior ocean flux is $-4.0 \pm 0.8 \text{ Pg C y}^{-1}$, $-3.1 \pm 0.5 \text{ Pg C y}^{-1}$,
677 and $-3.9 \pm 0.3 \text{ Pg C y}^{-1}$ for the three inversions, while it is $-1.6 \pm 0.5 \text{ Pg C y}^{-1}$, $-1.2 \pm 0.6 \text{ Pg C y}^{-1}$,
678 and $-1.5 \pm 0.8 \text{ Pg C y}^{-1}$ in the results of Houweling et al. (2015; pers. comm., 2016) (averaged
679 over different weighted averages of the models).

680 There is a strong negative correlation globally between posterior flux errors for land and
681 ocean of -0.84 and -0.89 in the in situ-only and the GOSAT-only inversion, respectively. Basu et
682 al. (2013) also reported a large negative correlation between land and ocean fluxes of -0.97 in
683 their in situ + GOSAT inversion during September 2009–August 2010. The anti-correlations
684 imply that the observations cannot adequately distinguish between adjustments in the global land
685 and ocean sinks. Thus, land-ocean error correlation may be a fundamental challenge that global
686 CO_2 flux inversions are faced with, at least given the sampling characteristics of the in situ and
687 GOSAT data sets used here. Without tight prior constraints on ocean fluxes, those fluxes are
688 subject to large, and potentially unrealistic, adjustments (i.e. dipole behavior).

689 To assess the effect of prior constraints on the inversion, we conducted a test with
690 reduced prior uncertainties, for both land and ocean fluxes, so that they are similar on average to
691 those of CT. Results for an in situ-only inversion and a GOSAT-only inversion are shown in
692 Table 1 and Fig. 12. For the in situ-only inversion, the posterior ocean flux is now much smaller
693 in magnitude, $-2.8 \pm 0.3 \text{ Pg C y}^{-1}$. The posterior ocean flux for the GOSAT inversion does not
694 change as much, decreasing in magnitude from the original $-3.1 \pm 0.5 \text{ Pg C y}^{-1}$ to $-2.9 \pm 0.2 \text{ Pg C}$
695 y^{-1} . The ocean flux 1σ ranges for both inversions now overlap with that of CT; accounting for
696 the riverine flux, the 1σ range for the in situ inversion overlaps with that of GCP, while the 1σ



697 range for the GOSAT inversion is still just outside of that of GCP. The inversions with tighter
698 priors generally exhibit better agreement with independent observations, e.g. lower-altitude
699 HIPPO observations (Fig. 13), and surface observations in the case of the GOSAT inversion
700 (Fig. 14), indicating that the effects of sampling and retrieval biases are reduced with tighter
701 prior uncertainties. The better agreement also lends support to the smaller ocean sink estimates.
702 (At high altitudes, keeping posterior mole fractions closer to the prior mole fractions results in
703 worse agreement with HIPPO in many places, especially for the GOSAT inversion.) However,
704 the tighter priors do not completely eliminate the discrepancies between the inversions and the
705 independent observations, suggesting that tight priors may not completely counteract the effects
706 of observational biases.

707 Basu et al. (2013) saw a similar underestimate of mole fractions during parts of the year
708 in the southern extratropics in their GOSAT inversion relative to surface observations and
709 overestimate of the seasonal cycle, though with some differences in the shape of the seasonal
710 cycle from our study (including a later descent toward and recovery from the annual minimum in
711 austral summer and a larger peak in late winter-early spring). They, however, used the SRON-
712 KIT RemoTeC GOSAT retrieval with a known issue over the ocean, and concluded that adding
713 global land and ocean observation bias correction terms to their inversion was needed to make
714 the land-ocean flux split more realistic and to improve the seasonal cycle of CO₂ in the southern
715 extratropics. In contrast, studies have found no noticeable bias in the ACOS B3.5 ocean glint
716 XCO₂ retrievals relative to TCCON (Kulawik et al., 2016) and a mean bias of only -0.06 ppm
717 relative to HIPPO (Frankenberg et al., 2016); the B3.4 version we use is on average ~0.2 ppm
718 lower than B3.5 in 2010 (Deng et al., 2016). So although a small overall negative bias in the
719 bias-corrected ACOS B3.4 ocean data cannot be ruled out, we conclude that the land-ocean flux



720 split in inversions using either in situ or GOSAT data is strongly influenced by error correlations
721 and dependent on the prior uncertainties assumed.

722 The shift in the global terrestrial sink from the tropics/south to the north when comparing
723 the GOSAT-only inversion with the in situ-only inversion and the prior is still seen when prior
724 uncertainties are decreased, as is a substantially larger global total budget in the GOSAT
725 inversion relative to the in situ (Fig. 12). The uncertainty reductions in the test inversions are
726 smaller than those in the baseline inversions (Table 1), as is expected from the smaller starting
727 values of the uncertainties. In summary, the magnitude of the ocean sink and the partitioning of
728 the global sink between land and ocean are sensitive to the prior uncertainties, but other inferred
729 features of the carbon budget are robust with respect to prior uncertainties.

730 Given that there is uncertainty in the land-ocean flux partitioning at sub-global scales as
731 well (e.g. as indicated by moderate negative correlations between northern land and northern
732 oceans, tropical land and tropical oceans, etc.), we consider results for combined land and ocean
733 regions in Figs. 8 and 12. They indicate that there is a shift in the global sink from the tropics to
734 the north and the south in the GOSAT inversion relative to the prior, and an increased source in
735 the tropics of $\sim 2 \text{ Pg C y}^{-1}$ in the GOSAT inversion relative to the in situ inversion. These
736 features are seen in the inversions with tighter priors as well as in the baseline inversions. Note
737 that the increased source over southern land and increased sink over southern ocean in the
738 GOSAT inversion relative to the in situ inversion that were discussed earlier cancel each other
739 out approximately, suggesting a compensation of errors.

740

741 3.4. Impacts of climatic conditions on 2009-2010 fluxes



742 We now analyze the impacts of several climatic events during the analysis period on CO₂
743 fluxes as indicated by the inversion results. We focus on 1) unusually hot and dry conditions at
744 Northern Hemisphere higher latitudes in summer of 2010, 2) wetter conditions over parts of
745 North America in spring and early summer of 2010 relative to 2009, and 3) record drought in the
746 Amazon in 2010.

747 Guerlet et al. (2013), who examined GOSAT data and performed a flux inversion using a
748 variational assimilation system, found that there was less net terrestrial CO₂ uptake in summer of
749 2010 than in 2009 at northern high latitudes, consistent with known severe heat waves, drought,
750 and high fire emissions, especially across Eurasia, centered around western Russia, and to a
751 lesser extent in North America.

752 Motivated by that study, we examined our inversion results for 2009 and 2010, focusing
753 on the GOSAT inversion. As can be seen in the global maps of natural plus biomass burning
754 fluxes in June-July-August (JJA) in Fig. 15, the GOSAT inversion does appear to exhibit a
755 decreased CO₂ uptake over Eurasia, including the area around western Russia (enclosed in a box
756 in the figure), in 2010. A decreased sink can also be seen in parts of North America. A
757 decreased sink over western Russia can also be seen in the CASA-GFED prior, though of a
758 smaller magnitude. In contrast, there is actually an increased sink in that region in the in situ
759 inversion. In fact, none of the sites used are in or immediately downwind of that region (Fig.
760 1a). Total NEP and fire fluxes over northern TC3 regions are shown in Fig. 16. There is less
761 CO₂ uptake in JJA 2010 than in 2009 in all the regions except Temperate Asia in the GOSAT-
762 only inversion. The differences exceed the 1 σ ranges for 3 of the 5 regions, even exceeding the
763 3 σ ranges for Europe, which includes western Russia. Also shown is the in situ + GOSAT
764 inversion, which exhibits a similar pattern of 2010-2009 differences. These inversion results are



765 thus consistent with the earlier GOSAT study. In contrast, the 2010-2009 differences in the prior
766 are small and, for some regions, of the opposite sign as that in the inversions (Fig. 16).

767 Measurements from the JR-STATION tower network are suitably located for evaluating
768 the inferred flux interannual variability over Eurasia. Time series are shown in Fig. 17 for
769 observations, the prior model, and the GOSAT-only inversion at 6 sites with complete
770 summertime data in 2009-2010. (As with the continuous measurements used in the in situ
771 inversion, afternoon data are selected to avoid difficulties associated with nighttime boundary
772 layers.) Posterior mole fractions are noisier in the wintertime, likely a result of the lack of
773 GOSAT observations during that season at these high latitudes. Focusing on 2010-2009
774 differences, the observations suggest a shallower drawdown in 2010 than in 2009 at most of the
775 sites, which is generally captured by both the prior and the GOSAT posterior. It appears though
776 that the GOSAT inversion exaggerates the 2010-2009 difference at some of the sites,
777 overestimating especially the drawdown in 2009. For a more quantitative analysis, we calculate
778 the average 2010-2009 difference in mole fractions over June-July-August for each site (Table
779 3). The GOSAT-only inversion overestimates the 2010-2009 difference at 5 of the 6 sites. The
780 in situ + GOSAT inversion exhibits less of an overestimate overall than the GOSAT-only
781 inversion, with 3 of the 6 sites being substantially overestimated. The prior exhibits the best
782 agreement with the observations overall.

783 The earlier study by Guerlet et al. (2013) assumed that the differences between 2010 and
784 2009 posterior biospheric fluxes are relatively insensitive to biases in the GOSAT data, since at
785 least some of those errors may be similar between the two years. However, our evaluation of the
786 inversions using JR-STATION data suggests that retrieval biases can vary significantly from
787 year to year. Kulawik et al. (2016) estimated a year-to-year variability in GOSAT biases relative



788 to TCCON of 0.3 ppm averaged over the stations. Another study has raised a separate but
789 related issue of inversion results potentially being sensitive to the spatiotemporal distribution of
790 observations in different data sets (e.g. different GOSAT retrievals) (H. Takagi, pers. comm.,
791 2015); by extension, comparison of fluxes from two time periods can be affected by changes in
792 the distribution of observations over time within a particular data set. But in JJA 2009 and 2010,
793 there are similar numbers of ACOS GOSAT observations overall in the northern land region, so
794 differences in data coverage are probably not a factor in this particular case study.

795 Our evaluation using JR-STATION data also indicates that the prior may be a reasonable
796 estimate of the 2010-2009 difference in growing season fluxes, at least over Siberia, despite
797 possible shortcomings in the simulation of drought impacts on NEP and of the overall magnitude
798 of fire emissions by CASA-GFED3. The latest version of GFED (version 4s), which includes
799 small fires, tends to generate higher emissions than GFED3 (van der Werf et al., 2017).

800 Over large parts of North America, conditions were wetter in spring and early summer of
801 2010 than in 2009, especially in the western half of the U.S. and adjacent parts of Mexico and
802 Canada, as suggested by North American drought maps for June 2010 vs. June 2009 (e.g.
803 <https://www.drought.gov/nadm/content/map/2010/06>) and shallow groundwater status maps for
804 the U.S. based on GRACE (Gravity Recovery and Climate Experiment) satellite data for May-
805 June (Houborg et al., 2012; <http://droughtcenter.unl.edu/NASA/GRACE/>). Consistent with the
806 wetter conditions in 2010 are a larger CO₂ sink over North America (Boreal + Temperate) in
807 May-June 2010 relative to 2009 in our priors (-5.0 ± 3.9 Pg C y⁻¹ vs. -3.4 ± 3.9 Pg C y⁻¹), in situ-
808 only posteriors (-5.0 ± 0.4 Pg C y⁻¹ vs. -3.8 ± 0.5 Pg C y⁻¹), and GOSAT-only posteriors ($-5.8 \pm$
809 0.4 Pg C y⁻¹ vs. -3.3 ± 1.8 Pg C y⁻¹). We consider the in situ inversion result to be reliable here,
810 given the large uncertainty reduction for North America and small error correlations with other



811 regions (not shown). The 2010 and 2009 fluxes differ such that their 1σ ranges do not overlap
812 for the in situ and the GOSAT posteriors. Despite the increased sink in June 2010 over North
813 America, the 2010 summer exhibits a decreased sink relative to 2009 when integrated through
814 JJA (Fig. 16).

815 The Amazon basin experienced a record drought in 2010, which led to decreased
816 vegetation greenness and a net carbon loss to the atmosphere (Xu et al., 2011; Gatti et al., 2014).
817 Dry conditions in the north and center of the basin in the first three months were caused by the El
818 Niño of late 2009-early 2010, and an enhanced and prolonged dry season in the southern areas of
819 the basin was connected to an Atlantic sea surface temperature anomaly during the second half
820 of the year (Gatti et al., 2014). According to our prior estimate, fire emissions minus NEP
821 represented a near-zero net flux of $-0.1 \pm 2.1 \text{ Pg C y}^{-1}$ in Jul-Sep 2010 (a period that includes
822 peak drought conditions and fire counts of that year) and a sink of $-1.9 \pm 2.1 \text{ Pg C y}^{-1}$ in Jul-Sep
823 2009 in the TC3 Tropical America region. (The fire emissions amounted to 2.0 Pg C y^{-1} and 0.2
824 Pg C y^{-1} in Jul-Sep 2010 and 2009, respectively, while NEP was 2.1 Pg C y^{-1} in both periods.)
825 However, our GOSAT inversion suggests the reverse, $-0.9 \pm 0.6 \text{ Pg C y}^{-1}$ vs. $-0.4 \pm 0.3 \text{ Pg C y}^{-1}$
826 for Jul-Sep 2010 and 2009, respectively. (We do not report the analogous results for the in situ
827 inversion, since the uncertainties are large in this undersampled region.) The prior estimate
828 seems more consistent with the expected impact of drought on fluxes than the inversion estimate
829 does. The inversion is hampered in the region by the relatively small number of GOSAT
830 soundings that are retrieved and pass the quality filters, especially during the burning season
831 (with substantial light scattering by aerosols) and the rainy season (with extensive cloud cover).
832 The dearth of observations results in relatively large posterior uncertainties and/or sizable flux
833 error correlations. Furthermore, there is differing data coverage, with 2010 having fewer



834 observations than 2009 in the TC3 Tropical America region during the height of the fire season
835 (85 and 20 in Aug and Sep 2010 vs. 101 and 33 in 2009) and more observations than 2009 in
836 July (150 vs. 85). The differing data coverage itself could affect the flux estimates differently in
837 2009 and 2010. The Amazonica data set does not enable an evaluation of the flux estimates for
838 both 2009 and 2010, since the data set begins in 2010. However, comparison of the prior and
839 GOSAT model mole fractions in 2010 with the Amazonica data shows that biases for both can
840 vary substantially over time, e.g. in July vs. Aug-Sep (Fig. S1). This raises the possibility that
841 neither the prior nor the GOSAT inversion correctly estimates the interannual flux difference in
842 this region and also supports the idea that inversion bias can vary with data coverage.

843

844

845 **4. Discussion and conclusions**

846 We have presented global, high-resolution, batch Bayesian CO₂ inversions using GOSAT
847 and in situ observations and compared them with flux estimates using Kalman filter and
848 variational approaches that involve various approximations. The exact inversion method
849 provides full posterior error covariances, which allows us to quantitatively evaluate the degree to
850 which regional fluxes are constrained independently of one another.

851 The GOSAT inversion is generally better constrained than the in situ inversion, with
852 smaller posterior regional flux uncertainties and correlations, except in places like North
853 America and high-latitude ocean where the in situ observation networks used provide relatively
854 good coverage. Note that our in situ inversion did not make use of all the surface monitoring
855 sites that operated during the analysis period, omitting for example a number of sites operated
856 exclusively by agencies in Canada, Australia, and Europe



857 (<http://ds.data.jma.go.jp/gmd/wdcgg/cgi-bin/wdcgg/catalogue.cgi>), and that the surface networks
858 have been enhanced with additional sites since then. Furthermore, the in situ data sets that we
859 used for evaluation of the inversions, including JR-STATION and Amazonica, could also be
860 used as input in the inversions. And yet other aircraft data sets and column measurements such
861 as from TCCON could be added. The use of GOSAT data in combination with in situ data
862 provides even greater flux uncertainty reductions than the use of either data set alone, indicative
863 of complementary constraints in the two datasets. Nevertheless, gaps in GOSAT sampling,
864 including a lack of observations at high latitudes during winter over land and year-round over the
865 ocean, and spatially, seasonally, and interannually varying coverage over tropical land, limit the
866 ability to accurately resolve fluxes down to the scale of TransCom sub-continental regions.

867 Our GOSAT inversion suggests a shift in the global terrestrial CO₂ sink from the tropics
868 and south to the north, relative to the prior and the in situ inversion; for combined land and ocean
869 fluxes, the GOSAT inversion produces a shift in the global sink from the tropics to the north and
870 the south relative to the prior, and an increased source in the tropics of $\sim 2 \text{ Pg C y}^{-1}$ relative to the
871 in situ inversion. Similar shifts are seen in studies using other inversion approaches, such as the
872 inversion intercomparison of Houweling et al. (2015). This result may be driven at least in part
873 by sampling and uncorrected retrieval biases in the ACOS GOSAT data set, as suggested by
874 sizable discrepancies between posterior mole fractions in the GOSAT-only inversion and surface
875 in situ and lower-tropospheric HIPPO aircraft observations. While the shift in the global sink
876 appears to be a robust feature of the inversions, the partitioning of the sink between land and
877 ocean in the inversions using either in situ or GOSAT data is found to be sensitive to prior
878 uncertainties because of negative correlations in the flux errors for the two domains. The loose
879 prior uncertainties assumed in our baseline inversions may explain the larger ocean sink



880 estimates compared to other studies, including CT2013B and the Houweling et al. (2015)
881 intercomparison. A rationale for specifying loose prior uncertainties is that this allows the
882 results to be driven more by the observations than by the prior estimates. However, in light of
883 increasing confidence in estimates of the global ocean sink (e.g. from GCP), it may be more
884 appropriate to start with a reliable set of ocean fluxes and apply tighter prior uncertainties similar
885 to those from our sensitivity test. In any case, more weight should be given to combined land
886 and ocean fluxes across latitudinal bands than to separate land and ocean flux estimates for the
887 current observational configurations. Gaps in coverage at higher latitudes, especially in winter,
888 as well as limited sampling over tropical land are a fundamental limitation of passive satellite
889 measurements (including OCO-2) and imply an important future role for active satellites such as
890 NASA's proposed Active Sensing of CO₂ Emissions over Nights, Days, and Seasons
891 (ASCENDS) mission (Kawa et al., 2010; ASCENDS Ad Hoc Science Definition Team, 2015).
892 Additional in situ and TCCON measurements in the tropics, especially in Africa, would also be
893 valuable for validating satellite retrievals and flux inversions using satellite data.

894 The GOSAT inversion indicates significantly less CO₂ uptake in summer of 2010 than in
895 2009 in the north, consistent with a previous GOSAT analysis and likely reflecting severe heat
896 waves and drought especially across Eurasia. However, observations from the JR-STATION in
897 situ network suggest that the GOSAT inversion (and to a lesser extent, the in situ + GOSAT
898 inversion) exaggerates the 2010-2009 difference in uptake in Siberia, while the CASA-GFED
899 prior reasonably estimates that quantity. Thus, it may not be accurate to assume that year-to-year
900 posterior flux differences are insensitive to satellite retrieval biases, as was done in the other
901 study. The prior, in situ posterior, and GOSAT posterior all indicate greater CO₂ uptake over
902 North America in spring to early summer of 2010 than in 2009, consistent with wetter conditions



903 over large parts of the continent. Decreased net uptake in July-September of 2010 relative to
904 2009 in our prior appears to be consistent with record drought in the Amazon in 2010, while the
905 GOSAT inversion shows the reverse. However, time-varying biases in both the prior model and
906 the GOSAT inversion relative to Amazon aircraft profiles raise the possibility that neither one
907 correctly estimates the interannual flux difference in this region and also support the idea that
908 inversion bias can vary with data coverage. Overall, the results do demonstrate that climatic
909 conditions can drive significant year-to-year variability in natural carbon fluxes on regional
910 scales.

911 This study has successfully applied the batch inversion method to satellite data at
912 relatively high resolution to generate a solution useful for comparison with other techniques.
913 However, for inversions over longer periods, using larger volumes of data such as from OCO-2,
914 or at higher flux resolution, more computationally efficient methods are essential.

915

916

917 **Competing interests**

918 The authors declare that they have no conflict of interest.

919

920 **Acknowledgments**

921 This work has been supported by the NASA Atmospheric CO₂ Observations from Space
922 program element and the NASA Carbon Monitoring System Program. The NASA Goddard
923 High-End Computing Program has provided access to and assistance with supercomputing
924 resources at the NASA Center for Climate Simulation. The ACOS GOSAT data were produced
925 by the ACOS/OCO-2 project at the Jet Propulsion Laboratory, California Institute of Technology



926 using spectra acquired by the GOSAT Project. We thank Chris O'Dell for providing the ACOS
927 data to us, John Miller and Manuel Gloor for their partnership in producing the Amazonica data
928 (with support from NERC, FAPESP, ERC, NASA, CNPQ, NOAA, IPEN, and U. of Leeds for
929 the Amazon Greenhouse measurement program led by L. Gatti), NOAA ESRL GMD CCGG for
930 making their flask and continuous tower data publicly available, JMA (including Yukio
931 Fukuyama and Atsushi Takizawa) for making their in situ data publicly available on the
932 WDCGG website and providing assistance, and Steven Wofsy for making HIPPO data available.
933 CT2013B results are provided by NOAA ESRL, Boulder, Colorado, USA from the website at
934 <http://carbontracker.noaa.gov>. Many thanks go to Martha Butler for providing inversion code
935 and documentation. We also thank Zhengxin Zhu for contributing to data processing, Liang
936 Feng and Paul Palmer for their inversion region map, David Baker for advice on inversions,
937 Sander Houweling for providing results from his intercomparison paper and for helpful
938 discussion, Lesley Ott for help with using ACOS data files and for discussions, Chris O'Dell, Ed
939 Dlugokencky, and especially Arlyn Andrews for comments on the manuscript, and Sourish Basu
940 and Brad Weir for discussions.

941

942



943 **References**

- 944 Andres, R. J., Boden, T. A., and Marland, G.: Monthly Fossil-Fuel CO₂ Emissions: Mass of
945 Emissions Gridded by One Degree Latitude by One Degree Longitude, Carbon Dioxide
946 Information Analysis Center, Oak Ridge National Laboratory, U.S. Department of Energy,
947 Oak Ridge, Tenn., U.S.A., doi:10.3334/CDIAC/ffe.MonthlyMass.2012, 2012.
- 948 Andrews, A. E., Kofler, J., Bakwin, P. S., Zhao, C., and Tans, P.: Carbon Dioxide and Carbon
949 Monoxide Dry Air Mole Fractions from the NOAA ESRL Tall Tower Network, 1992-2009,
950 Version: 2011-08-31, Path: <ftp://ftp.cmdl.noaa.gov/ccg/towers/>, 2009.
- 951 ASCENDS Ad Hoc Science Definition Team: Active Sensing of CO₂ Emissions over Nights,
952 Days, and Seasons (ASCENDS) Mission Science Mission Definition Study (draft),
953 https://cce.nasa.gov/ascends_2015/ASCENDS_FinalDraft_4_27_15.pdf, 2015.
- 954 Baker, D. F., Law, R. M., Gurney, K. R., Rayner, P., Peylin, P. and co-authors: TransCom 3
955 inversion intercomparison: Impact of transport model errors on the interannual variability of
956 regional CO₂ fluxes, 1988–2003, *Global Biogeochem. Cycles*, 20, GB1002,
957 doi:10.1029/2004GB002439, 2006.
- 958 Baldocchi, D., et al.: FLUXNET: A new tool to study the temporal and spatial variability of
959 ecosystem-scale carbon dioxide, water vapor, and energy flux densities, *Bull. Am. Meteorol.*
960 *Soc.*, 82, 2415–2434, 2001.
- 961 Basu, S., Guerlet, S., Butz, A., Houweling, S., Hasekamp, O., Aben, I., Krummel, P., Steele, P.,
962 Langenfelds, R., Torn, M., Biraud, S., Stephens, B., Andrews, A., and Worthy, D.: Global
963 CO₂ fluxes estimated from GOSAT retrievals of total column CO₂, *Atmos. Chem. Phys.*, 13,
964 8695–8717, doi:10.5194/acp-13-8695-2013, 2013.



- 965 Butler, M. P., Davis, K. J., Denning, A. S., and Kawa, S. R.: Using continental observations in
966 global atmospheric inversions of CO₂: North American carbon sources and sinks, *Tellus*,
967 62B, 550–572, doi:10.1111/j.1600-0889.2010.00501.x, 2010.
- 968 Chatterjee, A. and Michalak, A. M.: Technical Note: Comparison of ensemble Kalman filter and
969 variational approaches for CO₂ data assimilation, *Atmos. Chem. Phys.*, 13, 11643–11660,
970 doi:10.5194/acp-13-11643-2013, 2013.
- 971 Chevallier, F., et al.: What eddy-covariance measurements tell us about prior land flux errors in
972 CO₂-flux inversion schemes, *Global Biogeochem. Cycles*, 26, GB1021,
973 doi:10.1029/2010GB003974, 2012.
- 974 Chevallier, F., Palmer, P. I., Feng, L., Boesch, H., O'Dell, C. W., and Bousquet, P.: Toward
975 robust and consistent regional CO₂ flux estimates from in situ and spaceborne measurements
976 of atmospheric CO₂, *Geophys. Res. Lett.*, 41, 1065–1070, doi:10.1002/2013GL058772,
977 2013.
- 978 Ciais, P., Rayner, P., Chevallier, F., Bousquet, P., Logan, M., Peylin, P., and Ramonet, M.:
979 Atmospheric inversions for estimating CO₂ fluxes: methods and perspectives, *Climatic*
980 *Change*, 103:69–92, DOI 10.1007/s10584-010-9909-3, 2010.
- 981 Connor, B. J., Bösch, H., Toon, G., Sen, B., Miller, C., and Crisp, D.: Orbiting Carbon
982 Observatory: Inverse method and prospective error analysis, *J. Geophys. Res.*, 113, A05305,
983 doi:10.1029/2006JD008336, 2008.
- 984 Crisp, D.: Measuring atmospheric carbon dioxide from space with the Orbiting Carbon
985 Observatory-2 (OCO-2), *Proc. SPIE 9607, Earth Observing Systems XX*, 960702,
986 doi:10.1117/12.2187291, 2015.



- 987 Deng, F., Jones, D. B. A., Henze, D. K., Bousserez, N., Bowman, K. W., Fisher, J. B., Nassar,
988 R., O'Dell, C., Wunch, D., Wennberg, P. O., Kort, E. A., Wofsy, S. C., Blumenstock, T.,
989 Deutscher, N. M., Griffith, D. W. T., Hase, F., Heikkinen, P., Sherlock, V., Strong, K.,
990 Sussmann, R., and Warneke, T.: Inferring regional sources and sinks of atmospheric CO₂
991 from GOSAT XCO₂ data, *Atmos. Chem. Phys.*, 14, 3703–3727, doi:10.5194/acp-14-3703-
992 2014, 2014.
- 993 Deng, F., Jones, D. B. A., O'Dell, C. W., Nassar, R., and Parazoo, N. C.: Combining GOSAT
994 XCO₂ observations over land and ocean to improve regional CO₂ flux estimates, *J. Geophys.*
995 *Res. Atmos.*, 121, 1896–1913, doi:10.1002/2015JD024157, 2016.
- 996 Dlugokencky, E. J., Lang, P. M., Masarie, K. A., Crotwell, A. M., and Crotwell, M. J.:
997 Atmospheric Carbon Dioxide Dry Air Mole Fractions from the NOAA ESRL Carbon Cycle
998 Cooperative Global Air Sampling Network, 1968-2012, Version: 2013-08-28, available at:
999 ftp://aftp.cmdl.noaa.gov/data/trace_gases/co2/flask/surface/ (last access: 18 February 2014),
1000 2013.
- 1001 Engelen, R. J., Denning, A. S., and Gurney, K. R.: On error estimation in atmospheric CO₂
1002 inversions, *J. Geophys. Res.*, 107, 4635, doi:10.1029/2002JD002195, 2002.
- 1003 Enting, I. G. and Mansbridge, J. V.: Seasonal sources and sinks of atmospheric CO₂: Direct
1004 inversion of filtered data, *Tellus*, 41B, 111-126, 1989.
- 1005 Enting, I. G., Trudinger, C. M., and Francey, R. J.: A synthesis inversion of the concentration
1006 and $\delta^{13}\text{C}$ of atmospheric CO₂, *Tellus*, 47B, 35–52, 1995.
- 1007 Feng, L., Palmer, P. I., Boesch, H., and Dance, S.: Estimating surface CO₂ fluxes from space-
1008 borne CO₂ dry air mole fraction observations using an ensemble Kalman Filter, *Atmos.*
1009 *Chem. Phys.*, 9, 2619–2633, doi:10.5194/acp-9-2619-2009, 2009.



- 1010 Frankenberg, C., Kulawik, S. S., Wofsy, S., Chevallier, F., Daube, B., Kort, E. A., O'Dell, C.,
1011 Olsen, E. T., and Osterman, G.: Using airborne HIAPER Pole-to-Pole Observations (HIPPO)
1012 to evaluate model and remote sensing estimates of atmospheric carbon dioxide, Atmos.
1013 Chem. Phys., 16, doi:10.5194/acp-2015-961, 2016.
- 1014 Gatti, L. V., Gloor, M., Miller, J. B., Doughty, C. E., Malhi, Y., Domingues, L. G., Basso, L. S.,
1015 Martinewski, A., Correia, C. S. C., Borges, V. F., Freitas, S., Braz, R., Anderson, L. O.,
1016 Rocha, H., Grace, J., Phillips, O., and Lloyd, J.: Drought sensitivity of Amazonian carbon
1017 balance revealed by atmospheric measurements, Nature, 506, 76-80,
1018 doi:10.1038/nature12957, 2014.
- 1019 Gatti, L., Gloor, E., and Miller, J.: Greenhouse gas profile measurements (CO, CO₂, CH₄) above
1020 the forest canopy at four sites for the Amazonica project. NCAS British Atmospheric Data
1021 Centre, accessed 5 Dec 2016.
1022 <http://catalogue.ceda.ac.uk/uuid/7201536a8b7a1a96de584e9b746acee3>, 2016.
- 1023 Giglio, L., Csiszar, I., and Justice, C. O.: Global distribution and seasonality of active fires as
1024 observed with the Terra and Aqua Moderate Resolution Imaging Spectroradiometer
1025 (MODIS) sensors, J. Geophys. Res., 111, G02016, doi:10.1029/2005JG000142, 2006.
- 1026 Giglio, L., Randerson, J. T., van der Werf, G. R., Kasibhatla, P. S., Collatz, G. J., Morton, D. C.,
1027 and DeFries, R. S.: Assessing variability and long-term trends in burned area by merging
1028 multiple satellite fire products, Biogeosciences, 7, 1171–1186, doi:10.5194/bg-7-1171-2010,
1029 2010.
- 1030 GLOBALVIEW-CO₂: Cooperative Atmospheric Data Integration Project-Carbon Dioxide, CD-
1031 ROM, NOAA-ESRL, Boulder, Colo. [Also available on Internet via anonymous FTP to
1032 ftp.cmdl.noaa.gov,Path:ccg/co2/ GLOBALVIEW], 2009.



- 1033 Gourджи, S. M., Mueller, K. L., Yadav, V., Huntzinger, D. N., Andrews, A. E., Trudeau, M.,
1034 Petron, G., Nehrkorn, T., Eluszkiewicz, J., Henderson, J., Wen, D., Lin, J., Fischer, M.,
1035 Sweeney, C., and Michalak, A. M.: North American CO₂ exchange: intercomparison of
1036 modeled estimates with results from a fine-scale atmospheric inversion, *Biogeosciences*, 9,
1037 457–475, 2012.
- 1038 Guerlet, S., Basu, S., Butz, A., Krol, M., Hahne, P., Houweling, S., Hasekamp, O. P., and Aben,
1039 I.: Reduced carbon uptake during the 2010 Northern Hemisphere summer from GOSAT,
1040 *Geophys. Res. Lett.*, 40, 2378–2383, doi:10.1002/grl.50402, 2013.
- 1041 Gurney, K., Law, R., Rayner, P., and Denning, A. S.: TransCom 3 Experimental Protocol,
1042 Department of Atmospheric Science, Colorado State University, USA, Paper 707 (Available
1043 at http://transcom.colostate.edu/TransCom_3/transcom_3.html), 2000.
- 1044 Gurney, K. R., et al.: Towards robust regional estimates of CO₂ sources and sinks using
1045 atmospheric transport models, *Nature*, 415, 626–630, 2002.
- 1046 Gurney, K. R., Chen, Y.-H., Maki, T., Kawa, S. R., Andrews, A., and Zhu, Z.: Sensitivity of
1047 atmospheric CO₂ inversions to seasonal and interannual variations in fossil fuel emissions, *J.*
1048 *Geophys. Res.*, 110, D10308, doi:10.1029/2004JD005373, 2005.
- 1049 Hayes, D. J., Turner, D. P., Stinson, G., McGuire, A. D., Wei, Y., West, T. O., Heath, L. S.,
1050 deJong, B., McConkey, B. G., Birdsey, R. A., Kurz, W. A., Jacobson, A. R., Huntzinger, D.
1051 N., Pan, Y., Post, W. M., and Cook, R. B.: Reconciling estimates of the contemporary North
1052 American carbon balance among terrestrial biosphere models, atmospheric inversions, and a
1053 new approach for estimating net ecosystem exchange from inventory-based data, *Global*
1054 *Change Biology*, doi: 10.1111/j.1365-2486.2011.02627.x, 2012.



- 1055 Houborg, R., Rodell, M., Li, B., Reichle, R., and Zaitchik, B.: Drought indicators based on
1056 model assimilated GRACE terrestrial water storage observations, *Wat. Resour. Res.*, 48,
1057 W07525, doi:10.1029/2011WR011291, 2012.
- 1058 Houweling, S., Baker, D., Basu, S., Boesch, H., Butz, A., Chevallier, F., Deng, F., Dlugokencky,
1059 E. J., Feng, L., Ganshin, A., Hasekamp, O., Jones, D., Maksyutov, S., Marshall, J., Oda, T.,
1060 O'Dell, C. W., Oshchepkov, S., Palmer, P. I., Peylin, P., Poussi, Z., Reum, F., Takagi, H.,
1061 Yoshida, Y., and Zhuravlev, R.: An intercomparison of inverse models for estimating sources
1062 and sinks of CO₂ using GOSAT measurements, *J. Geophys. Res. Atmos.*, 120, 5253–5266,
1063 doi:10.1002/2014JD022962, 2015.
- 1064 Kaminski, T., Rayner, P. J., Heimann, M., and Enting, I. G.: On aggregation errors in
1065 atmospheric transport inversions, *J. Geophys. Res.*, 106, 4703–4715, 2001.
- 1066 Kawa, S. R., Erickson III, D. J., Pawson, S., and Zhu, Z.: Global CO₂ transport simulations using
1067 meteorological data from the NASA data assimilation system, *J. Geophys. Res.*, 109,
1068 D18312, doi:10.1029/2004JD004554, 2004.
- 1069 Kawa, S. R., Mao, J., Abshire, J. B., Collatz, G. J., Sun, X., and Weaver, C. J.: Simulation
1070 studies for a space-based CO₂ lidar mission, *Tellus B*, 62, 759-769, doi:10.1111/j.1600-
1071 0889.2010.00486.x, 2010.
- 1072 Kim, J., Kim, H. M., Cho, C.-H., Boo, K.-O., Jacobson, A. R., Sasakawa, M., Machida, T.,
1073 Arshinov, M., and Fedoseev, N.: Impact of Siberian observations on the optimization of
1074 surface CO₂ flux, *Atmos. Chem. Phys.*, 17, doi:10.5194/acp-17-2881-2017, 2017.
- 1075 Kulawik, S., Wunch, D., O'Dell, C., Frankenberg, C., Reuter, M., Oda, T., Chevallier, F.,
1076 Sherlock, V., Buchwitz, M., Osterman, G., Miller, C. E., Wennberg, P. O., Griffith, D.,
1077 Morino, I., Dubey, M. K., Deutscher, N. M., Notholt, J., Hase, F., Warneke, T., Sussmann,



- 1078 R., Robinson, J., Strong, K., Schneider, M., De Mazière, M., Shiomi, K., Feist, D. G., Iraci,
1079 L. T., and Wolf, J.: Consistent evaluation of ACOS-GOSAT, BESD-SCIAMACHY,
1080 CarbonTracker, and MACC through comparisons to TCCON, *Atmos. Meas. Tech.*, 9, 683–
1081 709, doi:10.5194/amt-9-683-2016, 2016.
- 1082 Law, R. M., et al.: TransCom model simulations of hourly atmospheric CO₂: Experimental
1083 overview and diurnal cycle results for 2002, *Global Biogeochem. Cycles*, 22, GB3009,
1084 doi:10.1029/2007GB003050, 2008.
- 1085 Le Quéré, C., Andres, R. J., Boden, T., Conway, T., Houghton, R. A., House, J. I., Marland, G.,
1086 Peters, G. P., van der Werf, G. R., Ahlström, A., Andrew, R. M., Bopp, L., Canadell, J. G.,
1087 Ciais, P., Doney, S. C., Enright, C., Friedlingstein, P., Huntingford, C., Jain, A. K., Jourdain,
1088 C., Kato, E., Keeling, R. F., Klein Goldewijk, K., Levis, S., Levy, P., Lomas, M., Poulter, B.,
1089 Raupach, M. R., Schwinger, J., Sitch, S., Stocker, B. D., Viovy, N., Zaehle, S., and Zeng, N.:
1090 The global carbon budget 1959–2011, *Earth Syst. Sci. Data*, 5, 165–185, doi:10.5194/essd-5-
1091 165-2013, 2013.
- 1092 Le Quéré, C., Moriarty, R., Andrew, R. M., Canadell, J. G., Sitch, S., Korsbakken, J. I.,
1093 Friedlingstein, P., Peters, G. P., Andres, R. J., Boden, T. A., Houghton, R. A., House, J. I.,
1094 Keeling, R. F., Tans, P., Arneeth, A., Bakker, D. C. E., Barbero, L., Bopp, L., Chang, J.,
1095 Chevallier, F., Chini, L. P., Ciais, P., Fader, M., Feely, R. A., Gkritzalis, T., Harris, I., Hauck,
1096 J., Ilyina, T., Jain, A. K., Kato, E., Kitidis, V., Klein Goldewijk, K., Koven, C.,
1097 Landschützer, P., Lauvset, S. K., Lefèvre, N., Lenton, A., Lima, I. D., Metzl, N., Millero, F.,
1098 Munro, D. R., Murata, A., Nabel, J., Nakaoka, S., Nojiri, Y., O'Brien, K., Olsen, A., Ono, T.,
1099 Pérez, F. F., Pfeil, B., Pierrot, D., Poulter, B., Rehder, G., Rödenbeck, C., Saito, S., Schuster,
1100 U., Schwinger, J., Séférian, R., Steinhoff, T., Stocker, B. D., Sutton, A. J., Takahashi, T.,



- 1101 Tilbrook, B., van der Laan-Luijkx, I. T., van der Werf, G. R., van Heuven, S., Vandemark,
1102 D., Viovy, N., Wiltshire, A., Zaehle, S., and Zeng, N.: Global Carbon Budget 2015. Earth
1103 System Science Data, 7:349-396. doi:10.5194/essd-7-349-2015, 2015.
- 1104 Lindqvist, H., et al.: Does GOSAT capture the true seasonal cycle of carbon dioxide?, Atmos.
1105 Chem. Phys., 15, 13023–13040, doi:10.5194/acp-15-13023-2015, 2015.
- 1106 Liu, J., Bowman, K. W., Lee, M., Henze, D. K., Bousseres, N., Brix, H., Collatz, G. J.,
1107 Menemenlis, D., Ott, L., Pawson, S., Jones, D., and Nassar, R.: Carbon monitoring system
1108 flux estimation and attribution: Impact of ACOS-GOSAT XCO₂ sampling on the inference of
1109 terrestrial biospheric sources and sinks, Tellus B, 66, 22,486, doi:10.3402/tellusb.v66.22486,
1110 2014.
- 1111 Los, S. O., Collatz, G. J., Sellers, P. J., Malmström, C. M., Pollack, N. H., DeFries, R. S.,
1112 Bounoua, L., Parris, M. T., Tucker, C. J., and Dazlich, D. A.: A global 9-yr biophysical land
1113 surface dataset from NOAA AVHRR data. J. Hydrometeorol., 1, 183–199, 2000.
- 1114 Maksyutov, S., et al.: Regional CO₂ flux estimates for 2009–2010 based on GOSAT and ground-
1115 based CO₂ observations, Atmos. Chem. Phys., 13, 9351–9373, 2013.
- 1116 Nassar, R., Jones, D. B. A., Suntharalingam, P., Chen, J. M., Andres, R. J., Wecht, K. J.,
1117 Yantosca, R. M., Kulawik, S. S., Bowman, K. W., Worden, J. R., Machida, T., and
1118 Matsueda, H.: Modeling global atmospheric CO₂ with improved emission inventories and
1119 CO₂ production from the oxidation of other carbon species, Geosci. Model Dev., 3, 689–716,
1120 doi:10.5194/gmd-3-689-2010, 2010.
- 1121 O'Dell, C. W., et al.: The ACOS CO₂ retrieval algorithm Part 1: Description and validation
1122 against synthetic observations, Atmos. Meas. Tech., 5, 99–121, 2012.



- 1123 Olsen, S. C. and Randerson, J. T.: Differences between surface and column atmospheric CO₂ and
1124 implications for carbon cycle research, *Journal of Geophysical Research*, 109, D02301,
1125 doi:10.1029/2003JD003968, 2004.
- 1126 Orbe, C., Holzer, M., Polvani, L. M., and Waugh, D.: Air-mass origin as a diagnostic of
1127 tropospheric transport, *J. Geophys. Res. Atmos.*, 118, 1459–1470, doi:10.1002/jgrd.50133,
1128 2013.
- 1129 Osterman, G., Eldering, A., Avis, C., O’Dell, C., Martinez, E., Crisp, D., Frankenberg, C., and
1130 Frankenberg, B.: ACOS Level 2 Standard Product Data User’s Guide, v3.4, Jet Propulsion
1131 Laboratory, Pasadena, California, 2013.
- 1132 Pan, Y., Birdsey, R. A., Fang, J., Houghton, R., Kauppi, P. E., Kurz, W. A., Phillips, O. L.,
1133 Shvidenko, A., Lewis, S. L., Canadell, J. G., Ciais, P., Jackson, R. B., Pacala, S., McGuire,
1134 A. D., Piao, S., Rautiainen, A., Sitch, S., and Hayes, D.: A Large and Persistent Carbon Sink
1135 in the World’s Forests, *Science*, 333, 988-993, doi: 10.1126/science.1201609, 2011.
- 1136 Parazoo, N. C., Denning, A. S., Kawa, S. R., Corbin, K. D., Lokupitiya, R. S., and Baker, I. T.:
1137 Mechanisms for synoptic variations of atmospheric CO₂ in North America, South America
1138 and Europe, *Atmos. Chem. Phys.*, 8, 7239-7254, <https://doi.org/10.5194/acp-8-7239-2008>,
1139 2008.
- 1140 Peters, W., Jacobson, A. R., Sweeney, C., Andrews, A. E., Conway, T. J., Masarie, K., Miller, J.
1141 B., Bruhwiler, L. M. P., Pétron, G., Hirsch, A. I., Worthy, D. E. J., van der Werf, G. R.,
1142 Randerson, J. T., Wennberg, P. O., Krol, M. C., and Tans, P. P.: An atmospheric perspective
1143 on North American carbon dioxide exchange: CarbonTracker, *PNAS*, 104, 18925-18930,
1144 2007.



- 1145 Pinzon, J. E. and Tucker, C. J.: A non-stationary 1981-2012 AVHRR NDVI_{3g} time series,
1146 Remote Sensing 6, 6929-6960; doi:10.3390/rs6086929, 2014.
- 1147 Randerson, J. T., Thompson, M. V., and Malmstrom, C. M.: Substrate limitations for
1148 heterotrophs: Implications for models that estimate the seasonal cycle of atmospheric CO₂,
1149 Global Biogeochem. Cycles, 10(4), 585–602, doi:10.1029/96GB01981, 1996.
- 1150 Rayner, P. J., Enting, I. G., Francey, R. J., and Langenfelds, R.: Reconstructing the recent carbon
1151 cycle from atmospheric CO₂, δ¹³C and O₂/N₂ observations, Tellus B, 51, 213–232, 1999.
- 1152 Reuter, M., et al.: Satellite-inferred European carbon sink larger than expected, Atmos. Chem.
1153 Phys. Discuss., 14, 21,829–21,863, doi:10.5194/acpd-14-21829-2014, 2014.
- 1154 Rienecker, M. M., Suarez, M. J., Gelaro, R., Todling, R., Bacmeister, J., Liu, E., Bosilovich, M.
1155 G., Schubert, S. D., Takacs, L., Kim, G.-K., Bloom, S., Chen, J., Collins, D., Conaty, A., Da
1156 Silva, A., Gu, W., Joiner, J., Koster, R. D., Lucchesi, R., Molod, A., Owens, T., Pawson, S.,
1157 Pegion, P., Redder, C. R., Reichle, R., Robertson, F. R., Ruddick, A. G., Sienkiewicz, M.,
1158 and Woollen, J.: MERRA: NASA's Modern-Era Retrospective Analysis for Research and
1159 Applications, J. Climate, 24, 3624–3648, 2011.
- 1160 Rodgers, C. D.: Inverse Methods for Atmospheric Sounding: Theory and Practice, World
1161 Scientific, Singapore, 2000.
- 1162 Saeki, T., Maksyutov, S., Saito, M., Valsala, V., Oda, T., Andres, R. J., Belikov, D., Tans, P.,
1163 Dlugokencky, E., Yoshida, Y., Morino, I., Uchino, O., and Yokota, T.: Inverse modeling of
1164 CO₂ fluxes using GOSAT data and multi-year ground-based observations, Sci. Online Lett.
1165 Atmos., 9, 45–50, doi:10.2151/sola.2013-011, 2013a.
- 1166 Saeki, T., Maksyutov, S., Sasakawa, M., Machida, T., Arshinov, M., Tans, P., Conway, T. J.,
1167 Saito, M., Valsala, V., Oda, T., Andres, R. J., and Belikov, D.: Carbon flux estimation for



- 1168 Siberia by inverse modeling constrained by aircraft and tower CO₂ measurements, J.
1169 Geophys. Res., 118, doi:10.1002/jgrd.50127, 2013b.
- 1170 Sasakawa, M., Shimoyama, K., Machida, T., Tsuda, N., Suto, H., Arshinov, M., Davydov, D.,
1171 Fofonov, A., Krasnov, O., Saeki, T., Koyama, Y., and Maksyutov, S.: Continuous
1172 measurements of methane from a tower network over Siberia, *Tellus B: Chemical and*
1173 *Physical Meteorology*, 62:5, 403-416, doi: 10.1111/j.1600-0889.2010.00494.x, 2010.
- 1174 Sasakawa, M., Machida, T., Tsuda, N., Arshinov, M., Davydov, D., Fofonov, A., and Krasnov,
1175 O.: Aircraft and tower measurements of CO₂ concentration in the planetary boundary layer
1176 and the lower free troposphere over southern taiga in West Siberia: Long-term records from
1177 2002 to 2011, *J. Geophys. Res.*, doi:10.1002/jgrd.50755, 2013.
- 1178 Schimel, D., Stephens, B. B., and Fisher, J. B.: Effect of increasing CO₂ on the terrestrial carbon
1179 cycle, *PNAS*, 112, doi/10.1073/pnas.1407302112, 2015.
- 1180 Stephens, B. B., et al.: Weak northern and strong tropical land carbon uptake from vertical
1181 profiles of atmospheric CO₂, *Science*, 316, 1732–1735, 2007.
- 1182 Takagi, H., et al.: On the benefit of GOSAT observations to the estimation of regional CO₂
1183 fluxes, *Sci. Online Lett. Atmos.*, 7, 161–164, 2011.
- 1184 Takagi, H., et al.: Influence of differences in current GOSAT XCO₂ retrievals on surface flux
1185 estimation, *Geophys. Res. Lett.*, 41, 2598–2605, doi:10.1002/2013GL059174, 2014.
- 1186 Takahashi, T., et al.: Climatological mean and decadal change in surface ocean pCO₂, and net
1187 sea-air CO₂ flux over the global oceans, *Deep Sea Res., Part II*, 56(8–10), 554–577, 2009.
- 1188 Tsutsumi, Y., Mori, K., Ikegami, M., Tashiro, T., and Tsuboi, K.: Long-term trends of
1189 greenhouse gases in regional and background events observed during 1998-2004 at



- 1190 Yonagunijima located to the east of the Asian continent, *Atmospheric Environment*, 40,
1191 5868-5879, 2006.
- 1192 van der Werf, G. R., Randerson, J. T., Giglio, L., Collatz, G. J., Kasibhatla, P. S., and Arellano
1193 Jr., A. F.: Interannual variability in global biomass burning emissions from 1997 to 2004,
1194 *Atmos. Chem. Phys.*, 6, 3423–3441, doi:10.5194/acp-6-3423-2006, 2006.
- 1195 van der Werf, G. R., Randerson, J. T., Giglio, L., Collatz, G. J., Mu, M., Kasibhatla, P. S.,
1196 Morton, D. C., DeFries, R. S., Jin, Y., and van Leeuwen, T. T.: Global fire emissions and the
1197 contribution of deforestation, savanna, forest, agricultural, and peat fires (1997–2009),
1198 *Atmos. Chem. Phys.*, 10, 11707–11735, doi:10.5194/acp-10-11707-2010, 2010.
- 1199 van der Werf, G. R., Randerson, J. T., Giglio, L., van Leeuwen, T. T., Chen, Y., Rogers, B. M.,
1200 Mu, M., van Marle, M. J. E., Morton, D. C., Collatz, G. J., Yokelson, R. J., and Kasibhatla,
1201 P. S.: Global fire emissions estimates during 1997–2016, *Earth Syst. Sci. Data*, 9, 697-720,
1202 doi:10.5194/essd-9-697-2017, 2017.
- 1203 Wofsy, S. C., et al.: HIAPER Pole-to-Pole Observations (HIPPO): fine-grained, global-scale
1204 measurements of climatically important atmospheric gases and aerosols, *Philos. T. R. Soc. A*,
1205 369, 2073–2086, doi:10.1098/rsta.2010.0313, 2011.
- 1206 Wofsy, S. C., et al.: HIPPO Merged 10-second Meteorology, Atmospheric Chemistry, Aerosol
1207 Data (R_20121129), Carbon Dioxide Information Analysis Center, Oak Ridge National
1208 Laboratory, Oak Ridge, Tennessee, U.S.A. http://dx.doi.org/10.3334/CDIAC/hippo_010
1209 (Release 20121129), 2012.
- 1210 Wunch, D., Wennberg, P. O., Toon, G. C., Connor, B. J., Fisher, B., Osterman, G. B.,
1211 Frankenberg, C., Mandrake, L., O'Dell, C., Ahonen, P., Biraud, S. C., Castano, R., Cressie,
1212 N., Crisp, D., Deutscher, N. M., Eldering, A., Fisher, M. L., Griffith, D. W. T., Gunson, M.,



- 1213 Heikkinen, P., Keppel-Aleks, G., Kyrö, E., Lindenmaier, R., Macatangay, R., Mendonca, J.,
1214 Messerschmidt, J., Miller, C. E., Morino, I., Notholt, J., Oyafuso, F. A., Rettinger, M.,
1215 Robinson, J., Roehl, C. M., Salawitch, R. J., Sherlock, V., Strong, K., Sussmann, R., Tanaka,
1216 T., Thompson, D. R., Uchino, O., Warneke, T., and Wofsy, S. C.: A method for evaluating
1217 bias in global measurements of CO₂ total columns from space, *Atmos. Chem. Phys.*, 11,
1218 12317–12337, doi:10.5194/acp-11-12317-2011, 2011.
- 1219 Xu, L., Samanta, A., Costa, M. H., Ganguly, S., Nemani, R. R., and Myneni, R. B.: Widespread
1220 decline in greenness of Amazonian vegetation due to the 2010 drought, *Geophys. Res. Lett.*,
1221 38, L07402, doi:10.1029/2011GL046824, 2011.
- 1222 Yokota, T., Yoshida, Y., Eguchi, N., Ota, Y., Tanaka, T., Watanabe, H., and Maksyutov, S.:
1223 Global concentrations of CO₂ and CH₄ retrieved from GOSAT: first preliminary results,
1224 *SOLA*, 5, 160–163, doi:10.2151/sola.2009-041, 2009.
- 1225



1226 **Table 1.** Inversion Prior and Posterior Fluxes and Uncertainties Aggregated to TransCom 3 Regions, June 2009–May 2010.

TransCom Region	Prior		Fires		In Situ-Only		GOSAT-Only ^b		In Situ + GOSAT		In Situ-Only, Tighter Prior		GOSAT-Only, Tighter Prior		U.R. (%)				
	Flux ^a	Unc	Flux	Unc	Flux	Unc	Flux	Unc	Flux	Unc	Flux	Unc	Flux	Unc					
Boreal North America	-0.1	0.6	0.1	0.1	0.1	0.1	81	0.2	0.3	43	0.1	0.1	87	-0.1	0.1	71	0.0	0.2	27
Temperate North America	-0.3	1.5	0.0	-0.6	0.1	0.1	93	-1.5	0.3	82	-0.7	0.1	96	-0.6	0.1	87	-1.2	0.2	71
Tropical America	0.4	1.0	0.1	-0.4	0.7	0.3	33	-0.2	0.2	79	-0.3	0.2	82	-0.2	0.3	26	-0.1	0.1	67
Temperate South America	0.4	1.2	0.1	0.4	0.8	0.3	31	1.1	0.2	85	1.0	0.2	85	0.3	0.3	27	0.9	0.1	73
Northern Africa	0.2	1.1	0.4	1.5	0.7	0.3	38	2.0	0.2	83	1.8	0.2	84	1.1	0.3	28	2.0	0.1	70
Southern Africa	0.0	1.2	0.8	-0.1	0.7	0.3	44	-0.6	0.1	89	-0.5	0.1	89	-0.1	0.3	38	-0.6	0.1	80
Boreal Asia	-0.1	1.2	0.1	-1.2	0.4	0.3	70	-0.5	0.4	65	-1.2	0.2	87	-1.0	0.2	60	-0.5	0.2	51
Temperate Asia	0.0	1.8	0.1	-0.1	0.7	0.3	61	1.4	0.4	79	0.9	0.3	85	-0.5	0.3	53	1.0	0.2	67
Tropical Asia	0.3	0.6	0.4	0.0	0.4	0.3	33	0.5	0.3	54	0.7	0.2	61	0.4	0.2	25	0.8	0.1	39
Australia	0.0	0.5	0.1	-0.2	0.4	0.3	15	0.6	0.2	71	0.3	0.1	73	-0.2	0.2	12	0.3	0.1	56
Europe	-0.1	1.3	0.0	0.6	0.4	0.3	70	-1.5	0.3	75	-0.6	0.2	87	0.3	0.2	61	-1.6	0.2	64
North Pacific Ocean	-0.5	0.3	0.0	-0.9	0.1	0.1	51	-0.5	0.2	29	-1.1	0.1	67	-0.8	0.1	29	-0.5	0.1	11
Tropical West Pacific Ocean	0.1	0.3	0.0	0.1	0.2	0.1	26	0.3	0.1	51	0.5	0.1	59	0.1	0.1	15	0.3	0.1	24
Tropical East Pacific Ocean	0.4	0.3	0.0	0.4	0.2	0.1	25	0.4	0.1	54	0.3	0.1	62	0.4	0.1	13	0.4	0.1	25
South Pacific Ocean	-0.3	0.6	0.0	-1.0	0.4	0.3	32	-1.1	0.3	51	-1.8	0.2	60	-0.6	0.2	18	-0.9	0.1	30
Arctic/Northern Ocean	-0.3	0.3	0.0	-0.4	0.1	0.1	56	-0.5	0.2	19	-0.1	0.1	62	-0.3	0.1	31	-0.4	0.1	5
North Atlantic Ocean	-0.2	0.2	0.0	-0.8	0.1	0.1	35	-0.5	0.1	23	-1.0	0.1	50	-0.5	0.1	12	-0.3	0.1	6
Tropical Atlantic Ocean	0.1	0.3	0.0	0.1	0.2	0.1	23	0.3	0.2	42	0.4	0.1	56	0.1	0.1	9	0.2	0.1	14
South Atlantic Ocean	-0.2	0.4	0.0	-0.5	0.3	0.3	19	-0.7	0.2	38	-1.0	0.2	49	-0.3	0.1	8	-0.5	0.1	18
Southern Ocean	-0.2	0.6	0.0	-0.4	0.3	0.3	48	-0.9	0.4	41	0.2	0.2	62	-0.5	0.1	34	-1.1	0.1	22
Tropical Indian Ocean	0.1	0.4	0.0	0.0	0.3	0.3	27	0.7	0.2	56	0.5	0.2	62	0.1	0.1	16	0.4	0.1	32
Southern Indian Ocean	-0.4	0.3	0.0	-0.5	0.2	0.1	15	-0.6	0.2	29	-0.6	0.2	40	-0.5	0.1	7	-0.4	0.1	11

^aFluxes in table, in Pg C, include fires but not fossil emissions

^bUncertainty reduction



1227 **Table 2.** Normalized Chi-Squared (Cost Function) Values for the Inversions.

Inversion	A Priori	A Posteriori
In situ only	112.4	4.0
GOSAT only	2.2	0.8
In situ + GOSAT	12.2	1.1
In situ only, decreased prior uncertainties	112.4	5.0
GOSAT only, decreased prior uncertainties	2.2	0.8

1228

1229

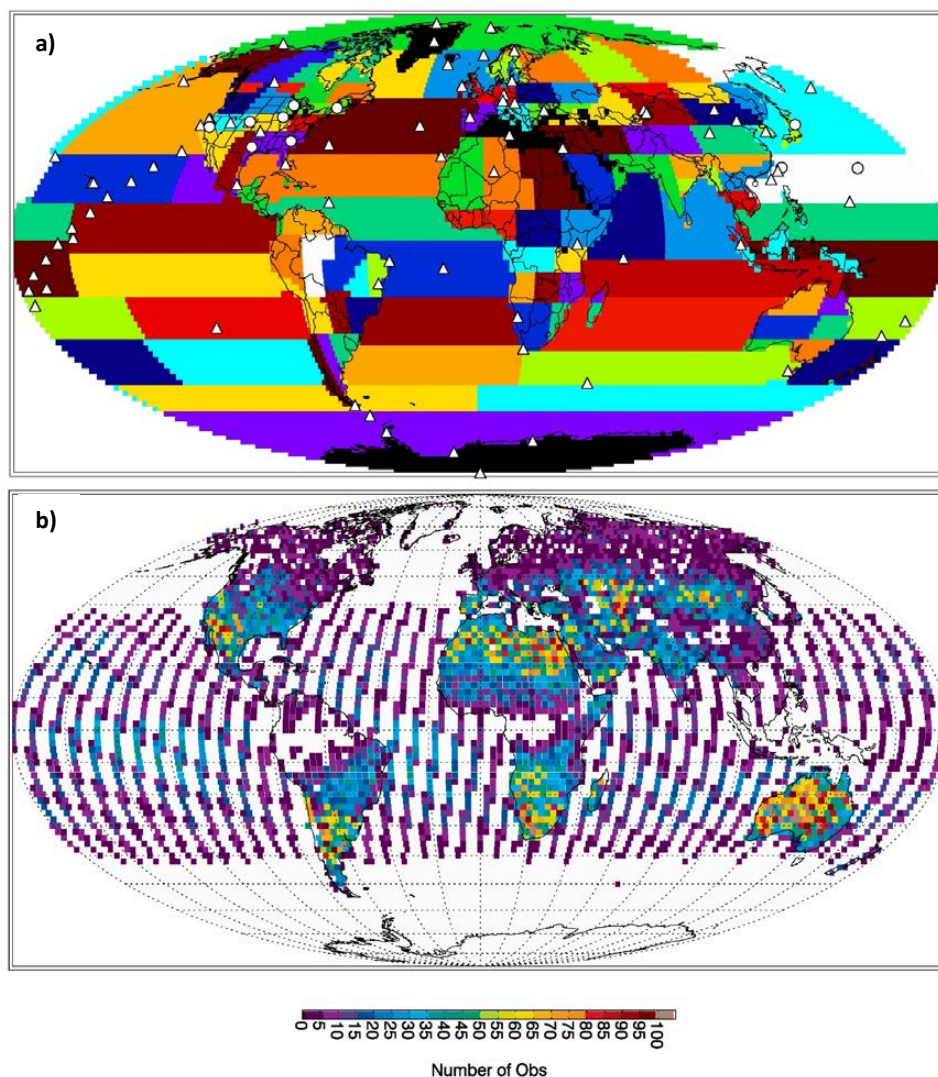


1230 **Table 3.** Mean 2010-2009 difference in mole fractions over June-July-August at Siberian sites

1231 (in ppm).

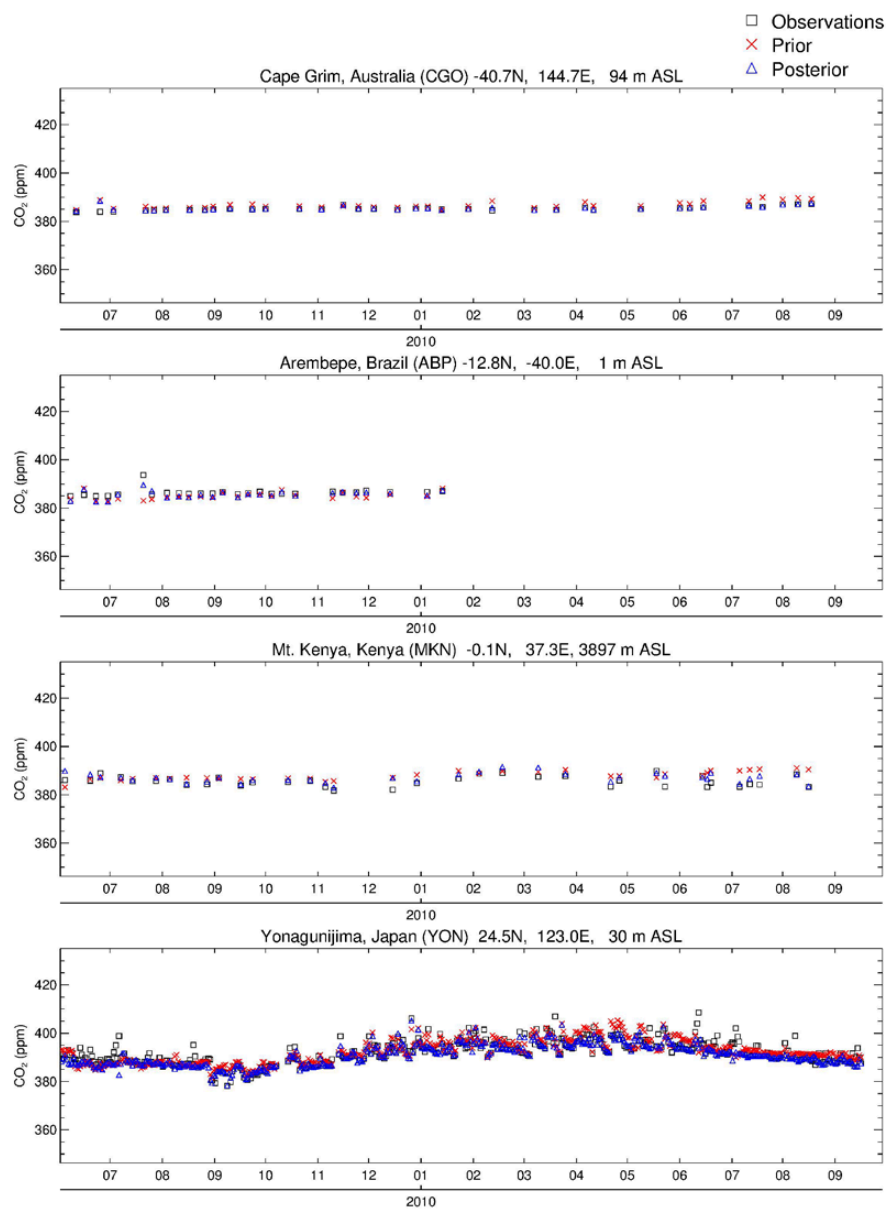
Site	Observations	Prior	GOSAT-Only Post	In Situ + GOSAT Post	Prior - Obs	(GOSAT-Only) - Obs	(In Situ + GOSAT) - Obs
VGN	5.2	5.3	7.4	6.6	0.1	2.2	1.4
AZV	7.0	6.3	8.1	7.1	-0.7	1.1	0.1
SVV	2.6	4.0	3.4	4.6	1.4	0.8	2.0
IGR	4.9	5.7	5.1	4.6	0.8	0.2	-0.3
KRS	6.6	5.4	3.8	3.2	-1.2	-2.8	-3.4
YAK	2.1	2.5	4.2	2.5	0.4	2.1	0.4

1232



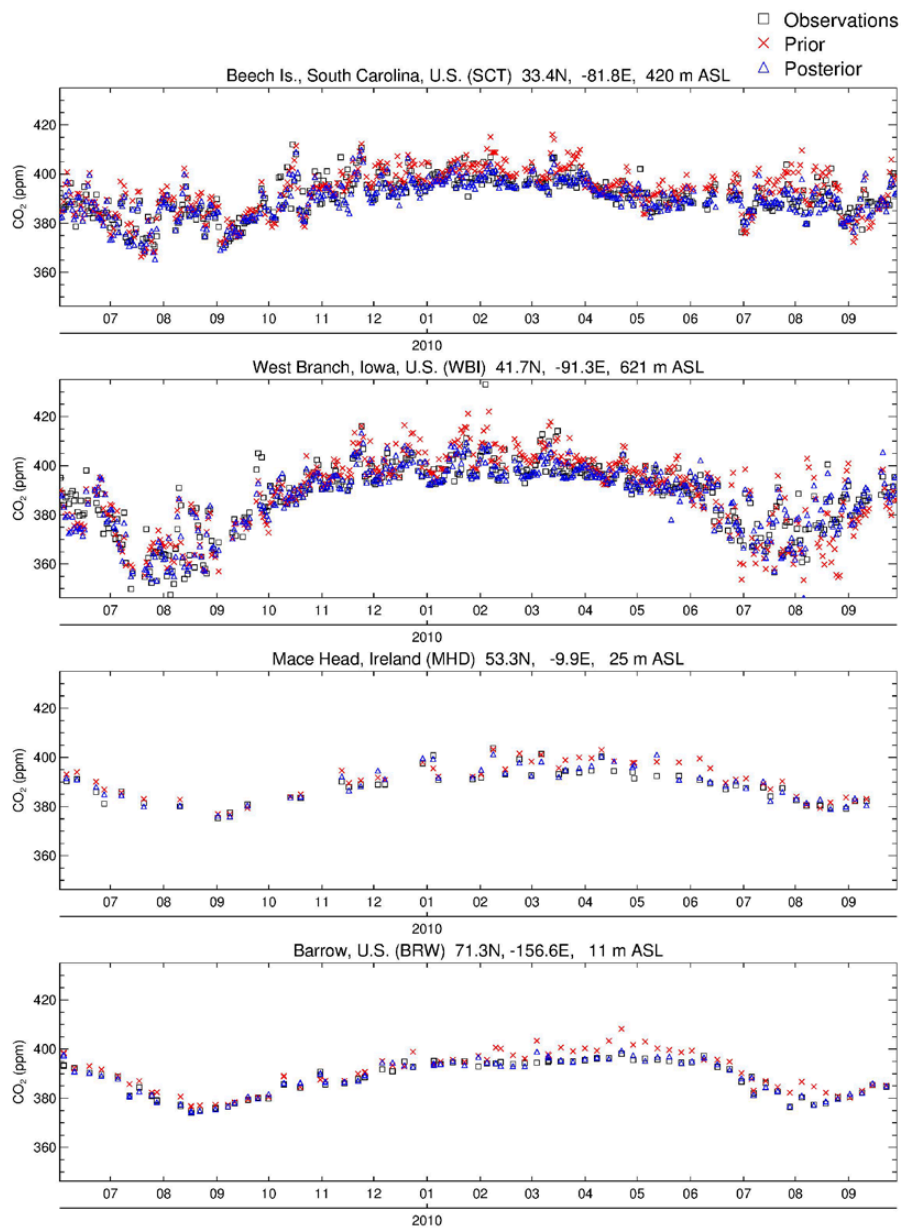
1233

1234 **Figure 1.** Locations of a) in situ observation sites and b) GOSAT XCO₂ observations used in the
1235 inversions. Also shown in a) are the 108 flux regions. Triangles in a) indicate flask sites, circles
1236 indicate continuous measurement sites. Observations in b) correspond to the ACOS B3.4
1237 retrieval, are filtered and averaged over each hour and 2° x 2.5° PCTM model grid column, and
1238 are shown for June 2009-May 2010.



1239

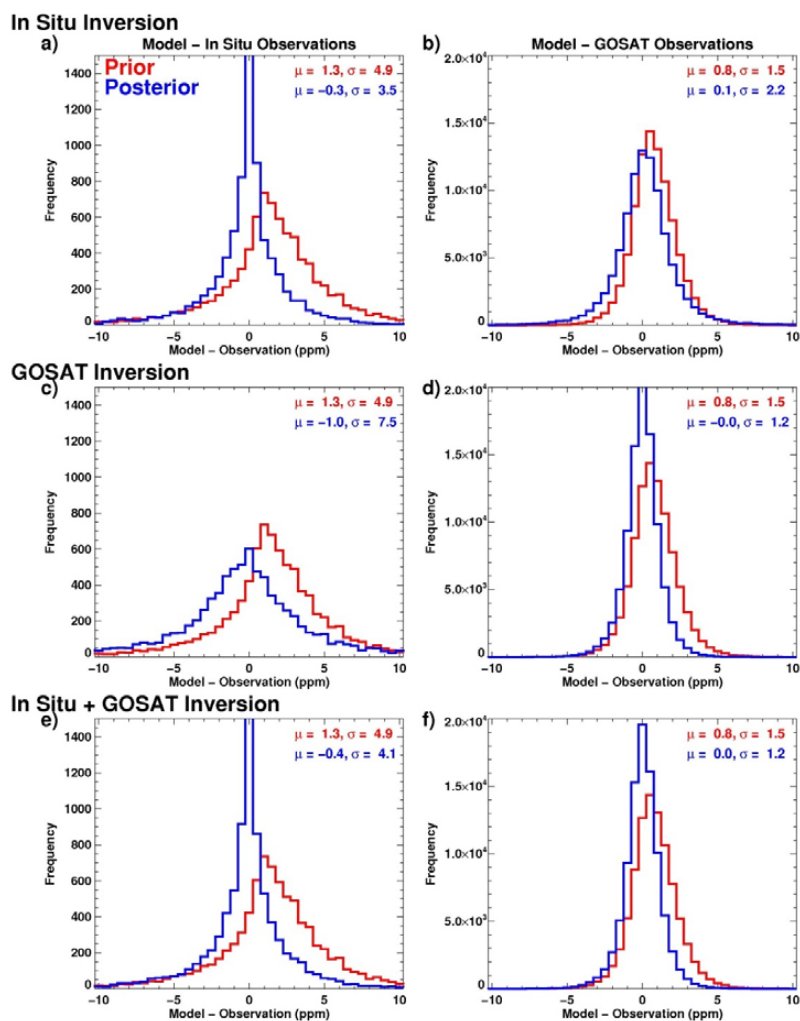
1240 **Figure 2.** Comparison of model and observed time series of CO₂ mole fractions at selected
1241 surface sites. Posterior mole fractions are for the in situ-only inversion. Sites are arranged from
1242 south to north. Elevations include intake heights on towers where applicable.



1243

1244 **Figure 2.** (continued)

1245

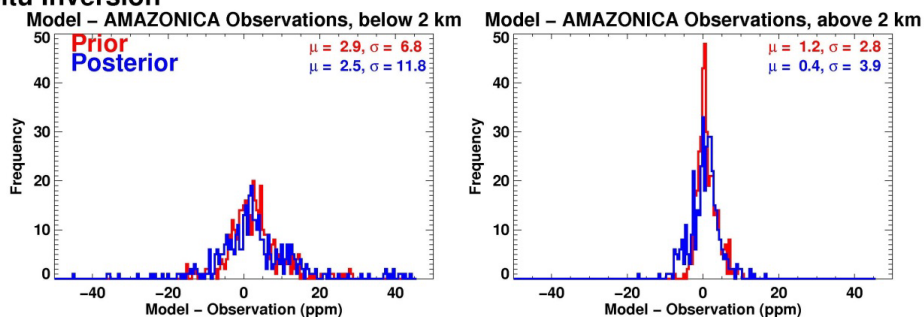


1246

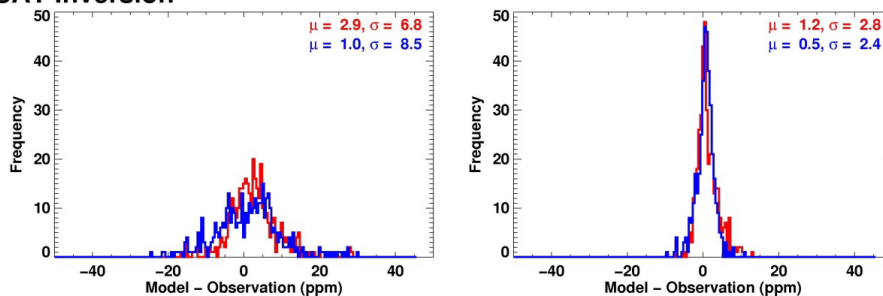
1247 **Figure 3.** Full comparison of model and observations. Model-observation difference histograms
1248 are shown for (a) in situ-only inversion and in situ observations, (b) in situ-only inversion and
1249 GOSAT observations, (c) GOSAT-only inversion and in situ observations, (d) GOSAT-only
1250 inversion and GOSAT observations, (e) in situ + GOSAT inversion and in situ observations, and
1251 (f) in situ + GOSAT inversion and GOSAT observations. Mean differences and standard
1252 deviations are indicated in the panels.



In Situ Inversion



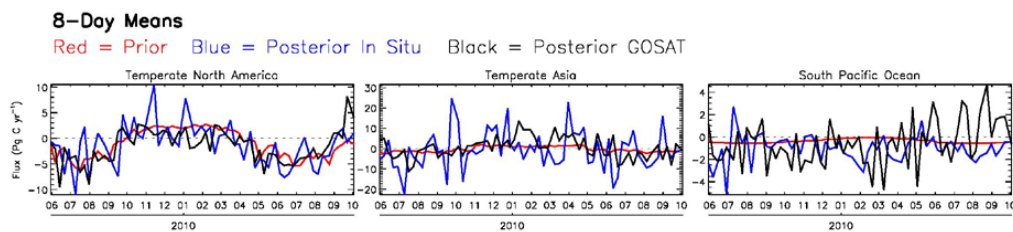
GOSAT Inversion



1253

1254 **Figure 4.** Comparison of model and Amazon aircraft observations (Amazonica project) over the
1255 period of overlap, Jan.-Sep. 2010. Top two panels show model-observation difference
1256 histograms for the in situ-only inversion and bottom two panels show results for the GOSAT-
1257 only inversion. Comparisons are shown separately for model and data below 2 km altitude (left)
1258 and above 2 km (right). Mean differences and standard deviations are indicated in the panels.

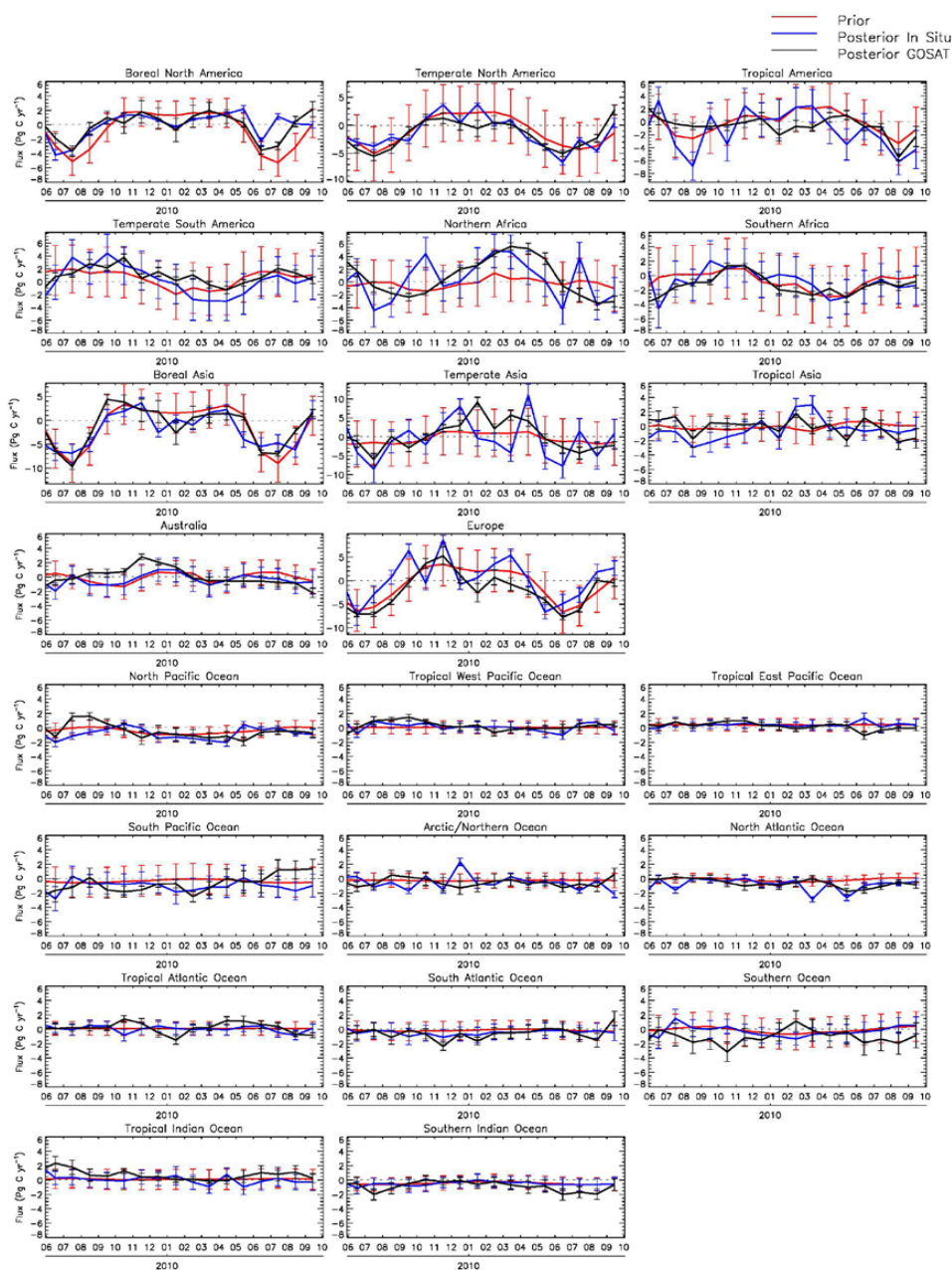
1259



1260

1261 **Figure 5.** Prior, posterior in situ-only, and posterior GOSAT-only 8-day mean NEP ($\times -1$) and
1262 ocean fluxes, aggregated over selected TransCom regions. Note that vertical scales are different
1263 in each of the panels.

1264



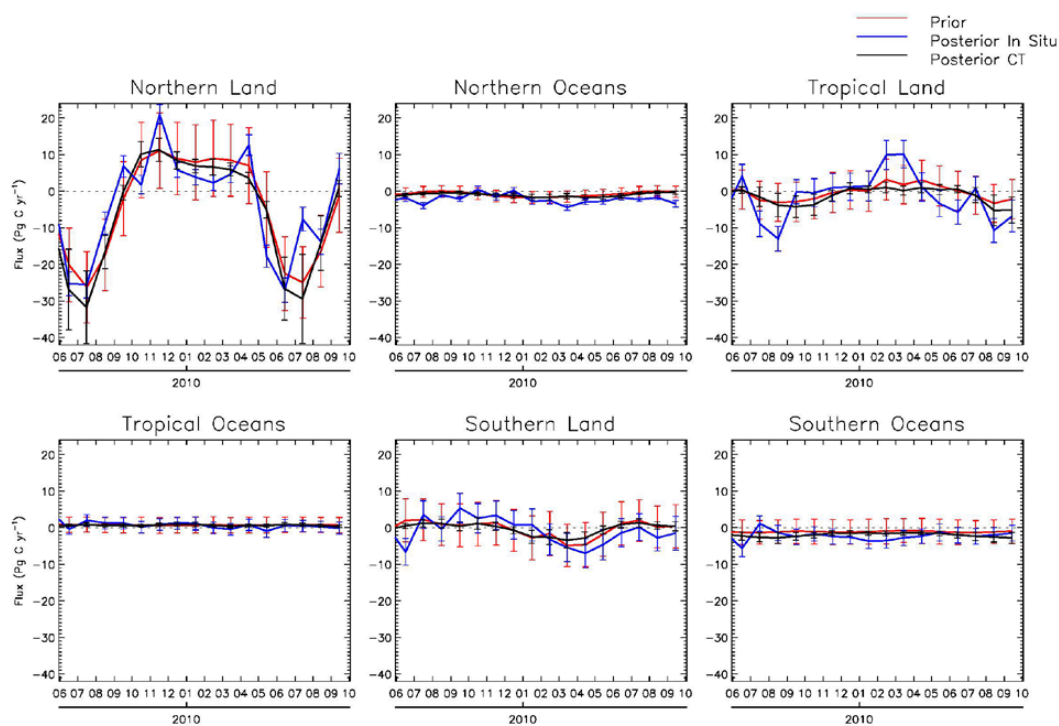
1265

1266 **Figure 6.** Same as Fig. 5, except showing monthly means of fluxes for all TransCom regions,

1267 with error bars that represent 1σ uncertainties.



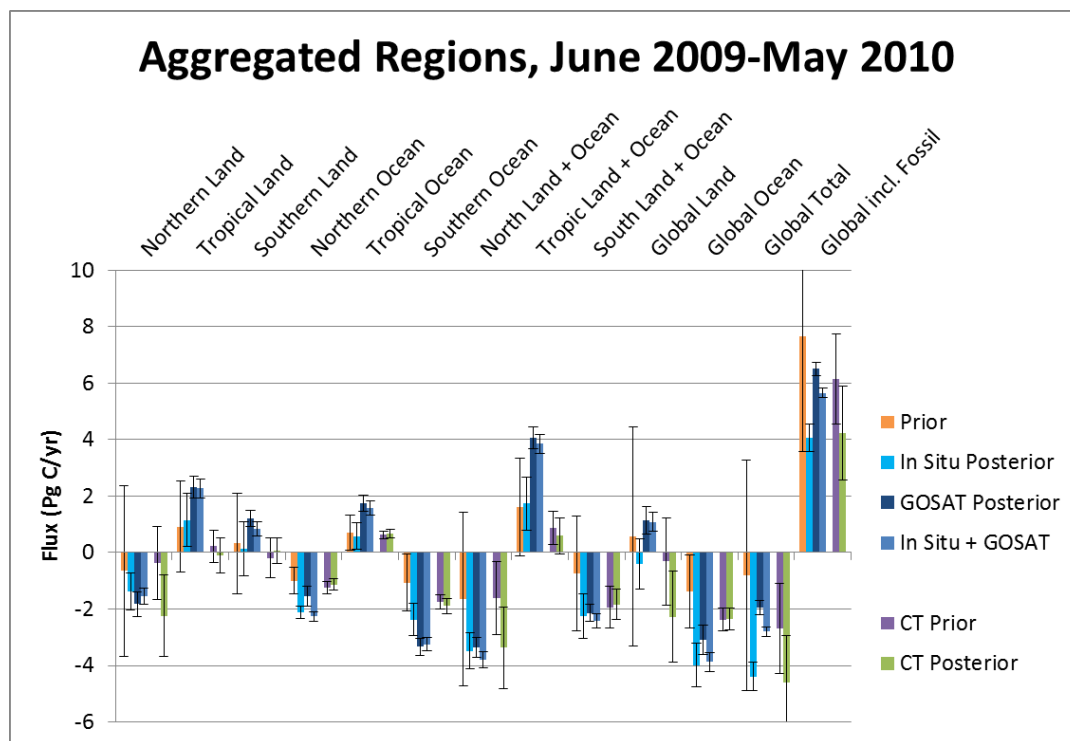
1268



1269

1270 **Figure 7.** Comparison of our in situ-only inversion monthly mean NEP ($\times -1$) and ocean fluxes,
1271 aggregated over large regions (as defined in TC3), with posterior fluxes from NOAA's
1272 CarbonTracker (CT2013B) data assimilation system. The priors shown are from our analysis;
1273 CT2013B priors are similar. Error bars represent 1σ uncertainties.

1274



1275

1276 **Figure 8.** Twelve-month mean NEP ($\times -1$), fire, and ocean fluxes aggregated over large regions.

1277 Included are results for the in situ-only, GOSAT-only, and in situ + GOSAT inversions as well

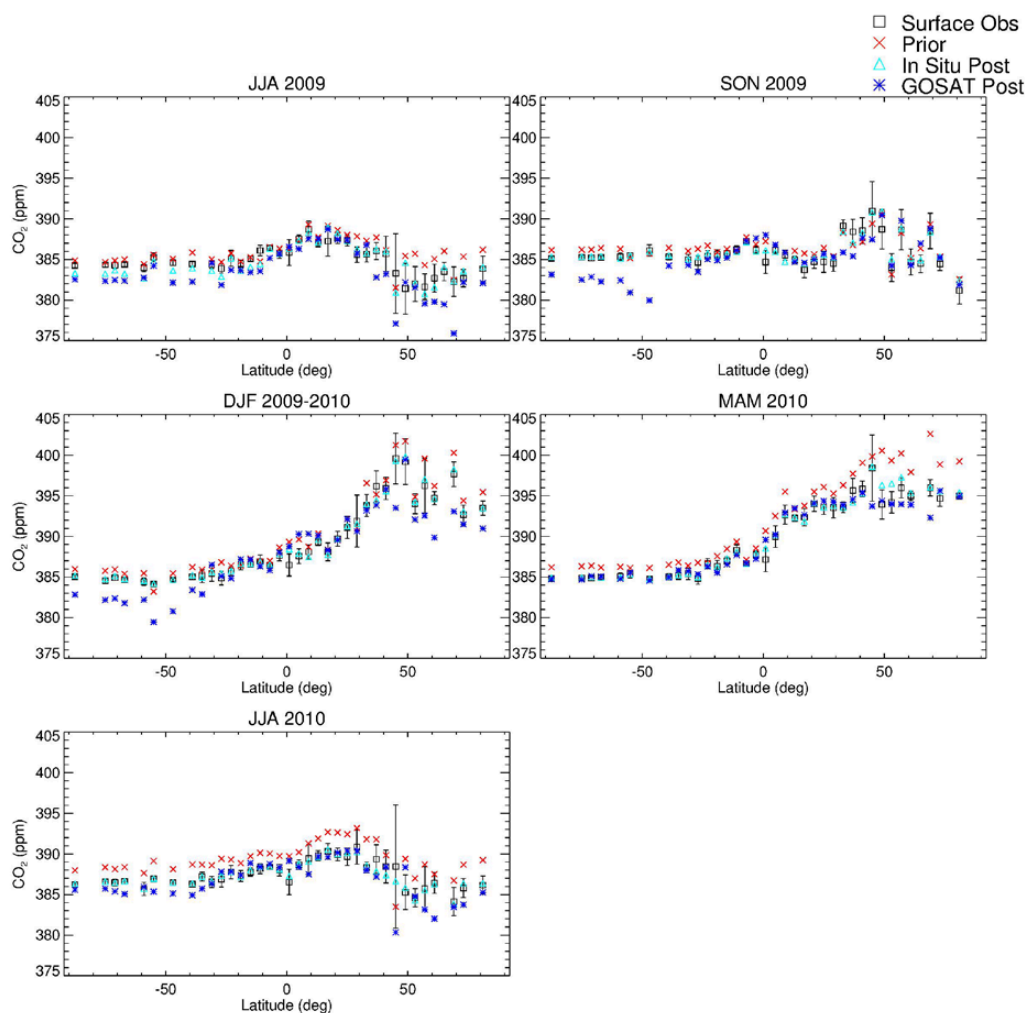
1278 as priors. Shown for comparison are priors and posteriors from CT2013B. Error bars represent

1279 1σ uncertainties; for CT2013B, “external” (across a set of priors) as well as “internal” (within a

1280 particular inversion) uncertainties are included. In summing monthly CT2013B fluxes over the

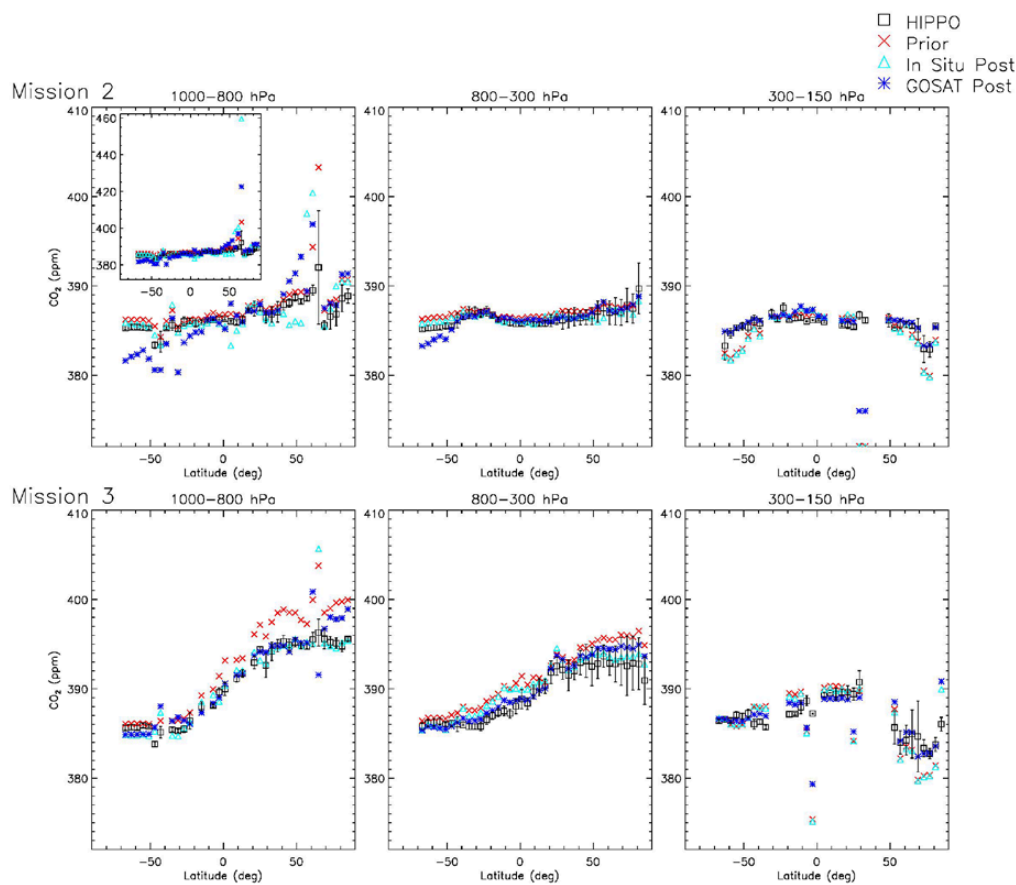
1281 12 months, we assumed zero error correlation between months.

1282



1283

1284 **Figure 9.** Latitudinal profiles of seasonal mean CO₂ mole fractions at surface sites for
1285 observations, prior, in situ-only posterior, and GOSAT-only posterior. Values are averaged in 4°
1286 bins. Error bars account for the spread of the observations within each season and bin as well as
1287 the uncertainty of each observation.

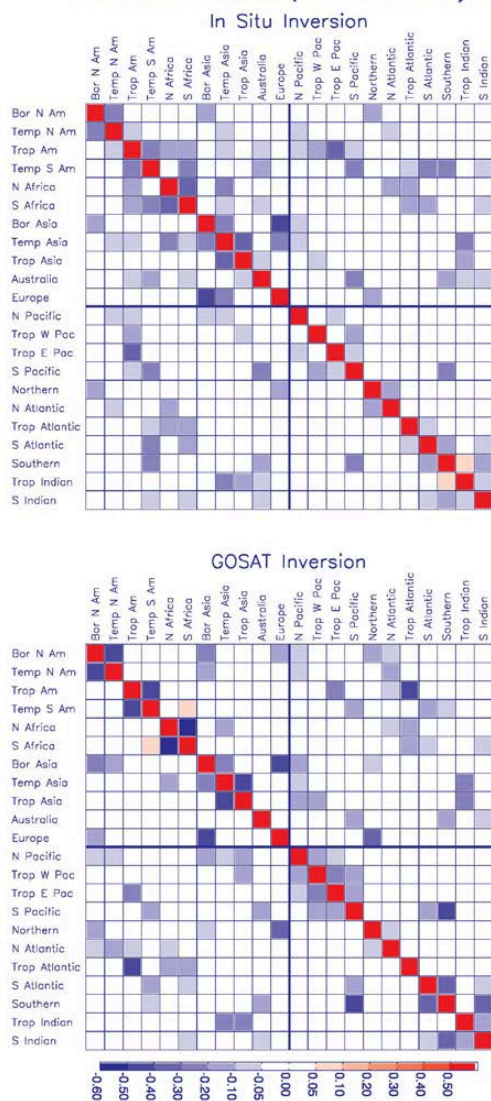


1288

1289 **Figure 10.** Latitudinal profiles of CO₂ mole fractions for HIPPO observations and co-sampled
1290 prior, in situ-only posterior, and GOSAT-only posterior. Mission 2 took place during Oct 31-
1291 Nov 22, 2009; Mission 3 took place Mar 24-Apr 16, 2010. Values are averaged in three altitude
1292 bins and 4° latitude bins. The inset in the first panel contains an expanded y-axis range that
1293 shows two points that do not fit into the default range. Flight segments over the temperate North
1294 American continent (east of -130°) are excluded from this comparison in order to focus on the
1295 Pacific. Error bars represent the standard deviations of the observations within each bin.



Posterior Correlations (June 2009 – May 2010)

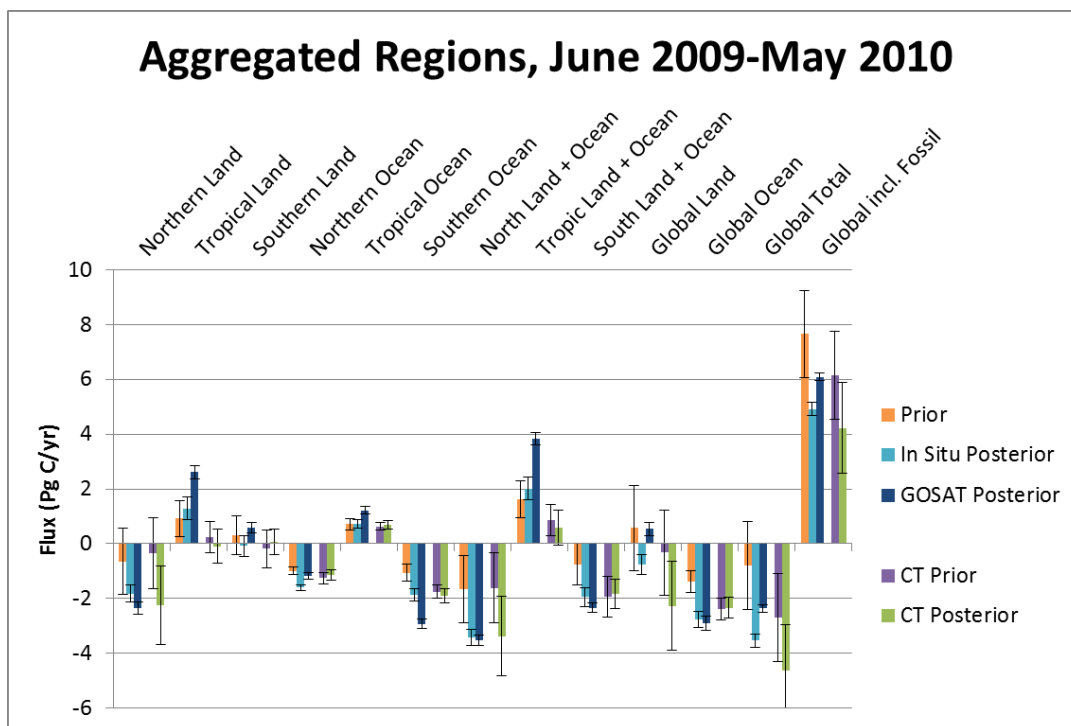


1296

1297 **Figure 11.** Posterior flux error correlations, aggregated to TC3 regions and a 12-month period,
 1298 for (a) the in situ-only inversion, and (b) the GOSAT-only inversion. The correlation is equal to
 1299 the error covariance divided by the product of the corresponding flux uncertainties (σ). Values
 1300 on the main diagonal are equal to 1.



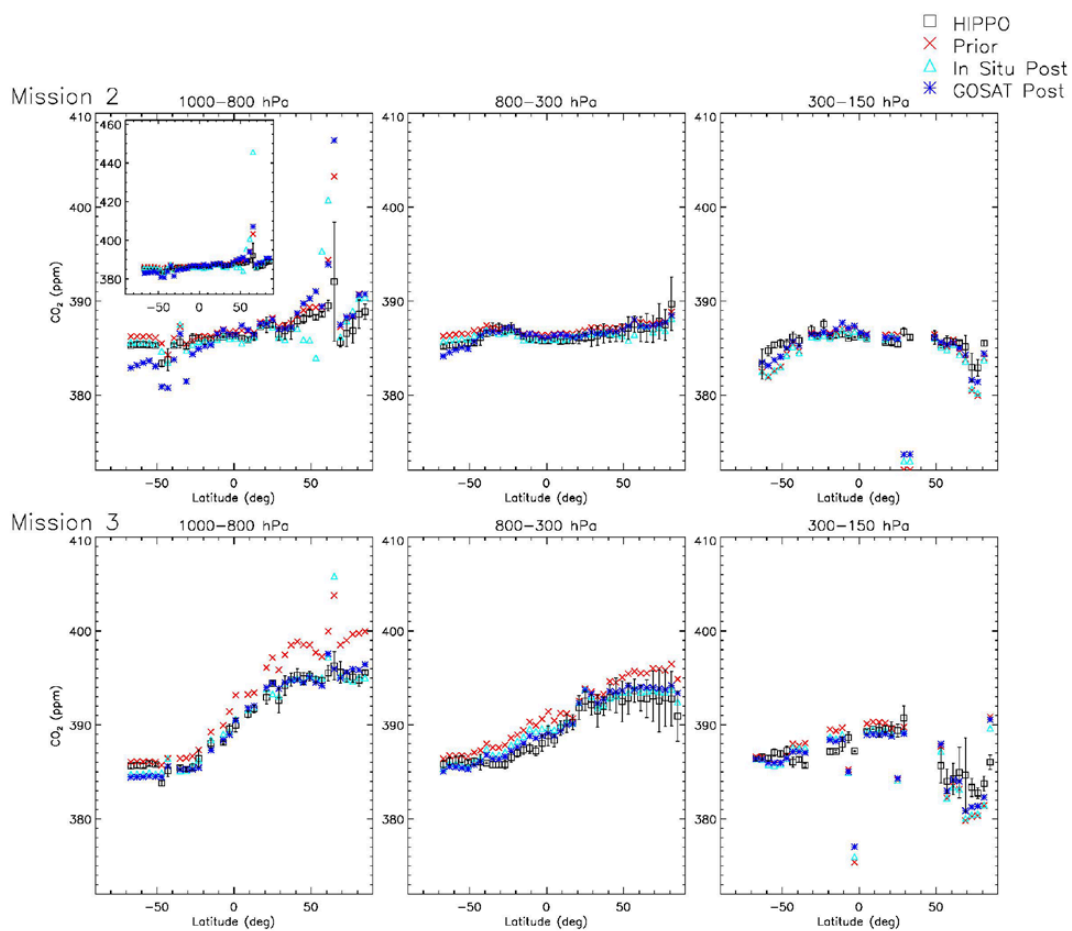
1301



1302

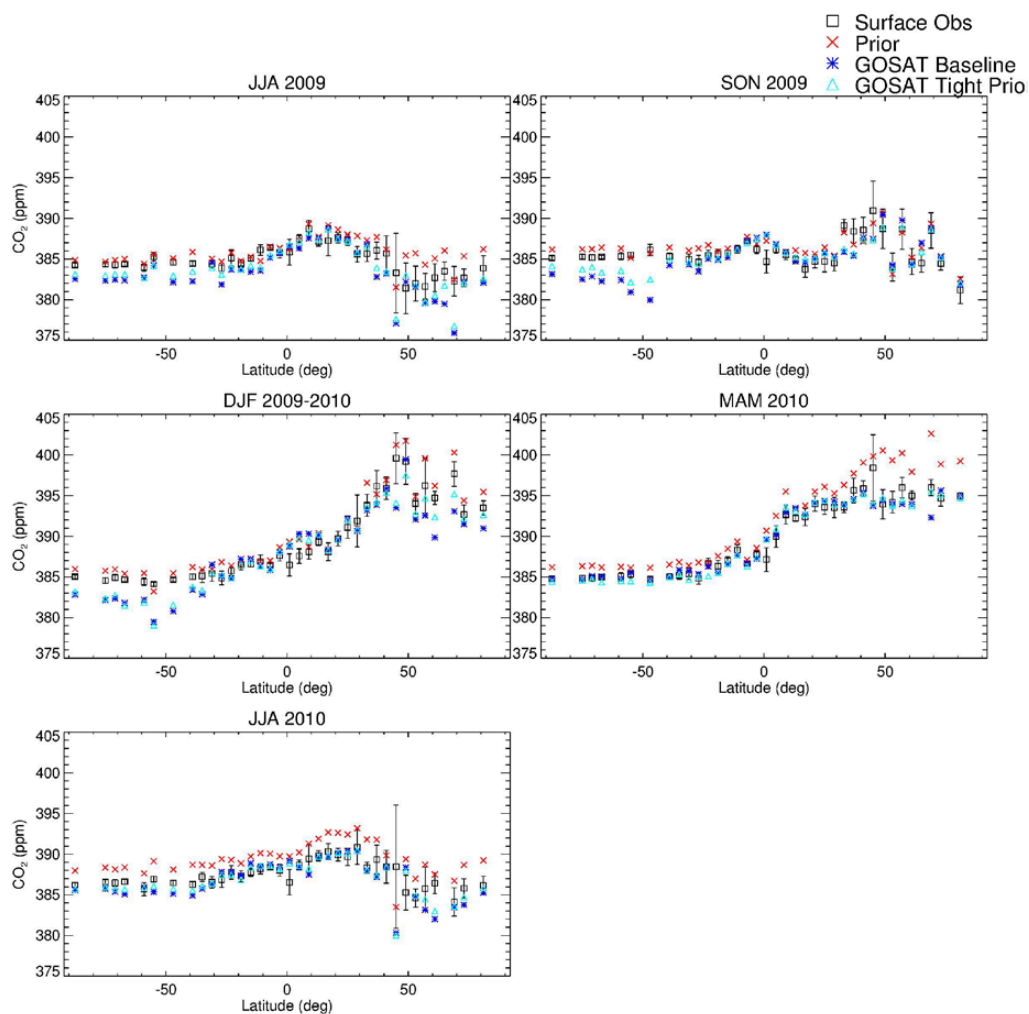
1303 **Figure 12.** Similar to Fig. 8, except showing results for inversions with tighter prior constraints
1304 (with prior uncertainties similar to CarbonTracker's). Included are results for the in situ-only
1305 and GOSAT-only inversions. CT2013B results shown in Fig. 8 are repeated here. Error bars
1306 represent 1σ uncertainties.

1307



1308

1309 **Figure 13.** Same as Fig. 10 except showing inversions with tighter prior uncertainties.

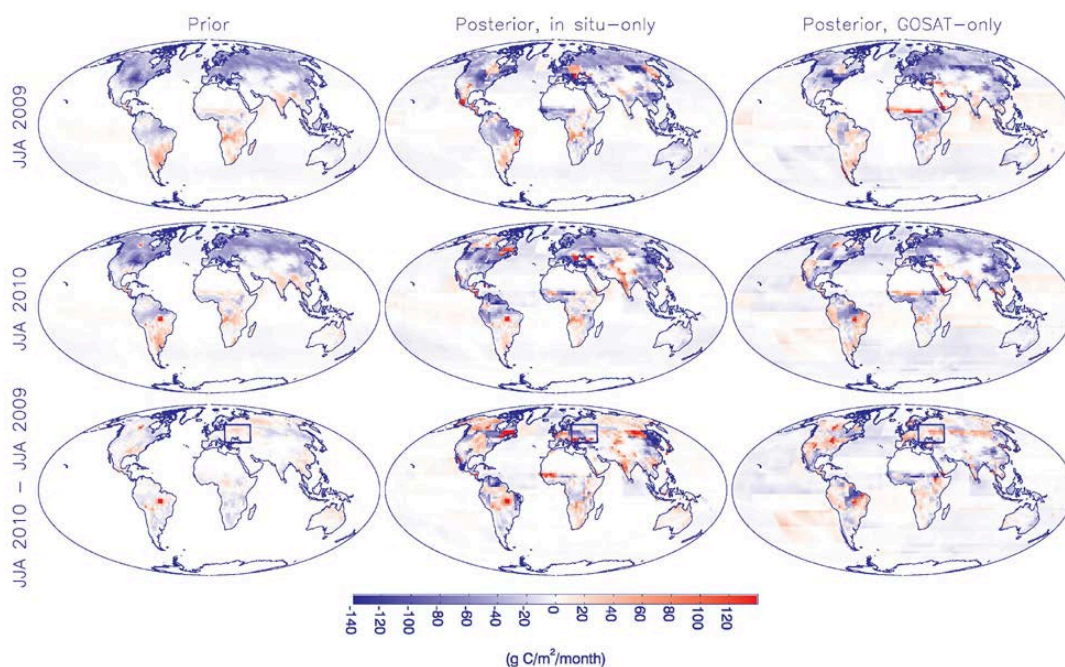


1310

1311 **Figure 14.** Same as Fig. 9 except showing GOSAT-only inversions with baseline vs. tighter

1312 prior uncertainties.

1313



1314

1315 **Figure 15.** Comparison of spatial distribution of fluxes for June-July-August of 2010 vs. 2009.

1316 Included are natural and fire fluxes. Shown are fluxes for 2009 (top), 2010 (middle), and the

1317 2010-2009 difference (bottom), for the priors (left), in situ-only inversion (middle), and GOSAT-

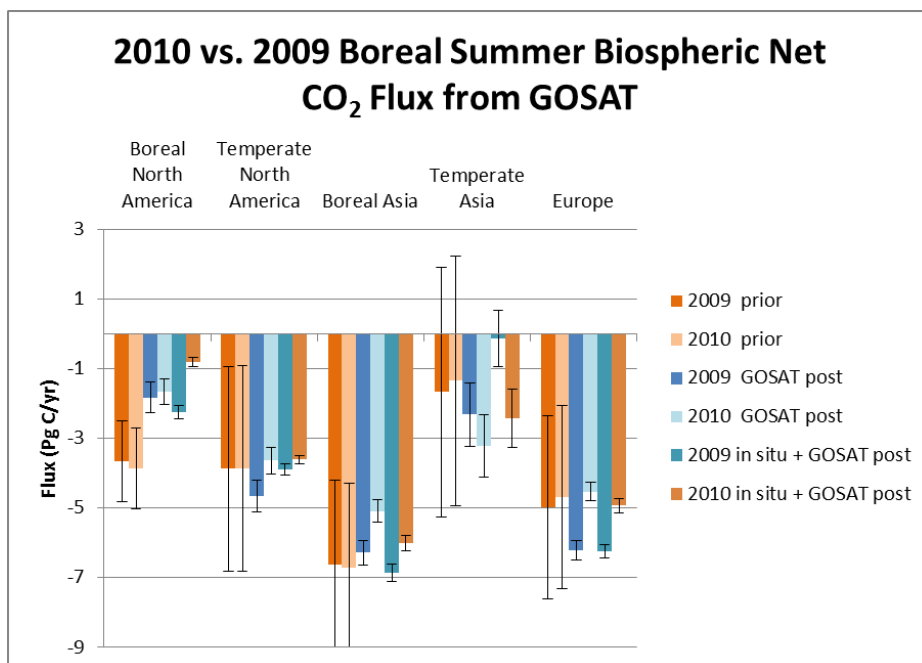
1318 only inversion (right). In the bottom row, boxes enclose the region around western Russia where

1319 there were intense heat waves, severe drought, and extensive fires. Note that the grid-scale

1320 spatial variability shown is not optimized in the inversions, so only patterns at the scale of the

1321 108 flux regions contain information from the observations.

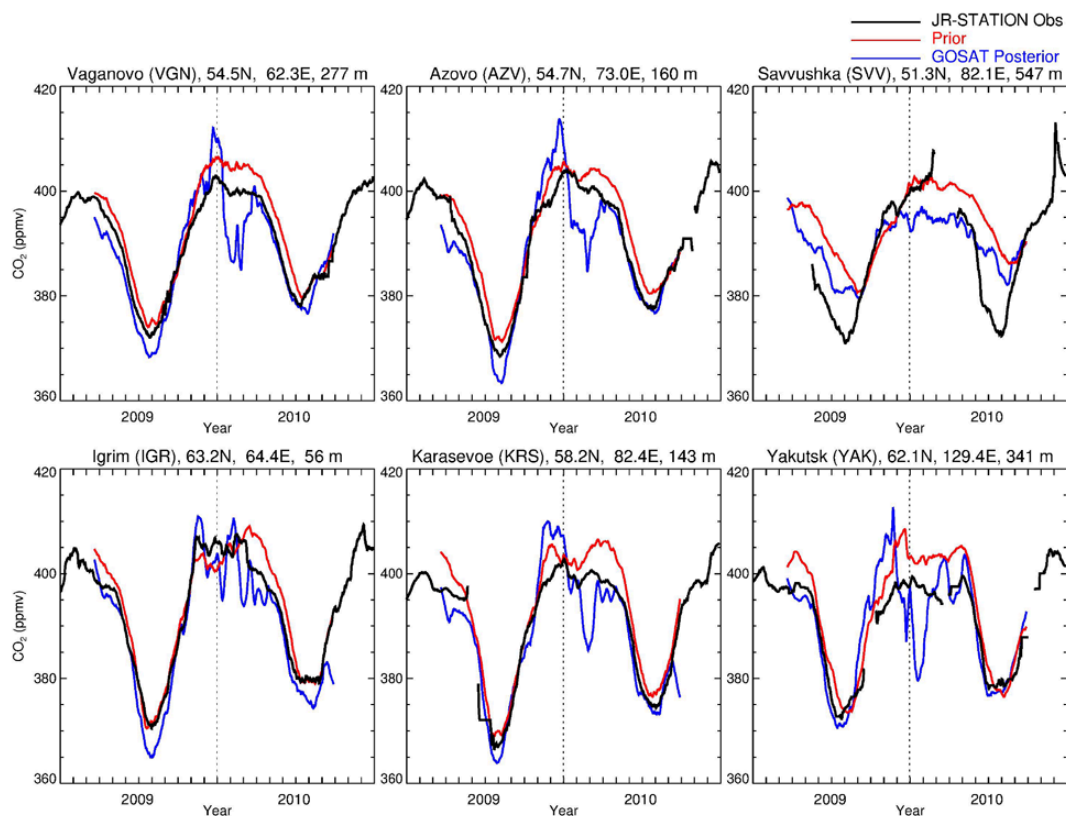
1322



1323

1324 **Figure 16.** Comparison of prior, GOSAT-only posterior, and in situ + GOSAT posterior fluxes
1325 aggregated over northern regions for June-July-August of 2010 vs. 2009. Included are NEP (\times -
1326 1) and fire fluxes. Error bars represent 1σ uncertainties.

1327



1328

1329 **Figure 17.** Evaluation of the prior model and GOSAT-only inversion against JR-STATION in
1330 situ observations in Siberia. Shown are daily afternoon average (1200-1700 local time) mole
1331 fractions from the highest level on each tower, the time series of which are smoothed with a 31-
1332 day window. Sites are arranged from west to east, first at lower latitudes and then at higher
1333 latitudes, excluding those with data gaps in the summer. Elevations shown include intake
1334 heights on towers.